Crustal deformation dynamics and stress evolution during seamount subduction: High-resolution 3-D numerical modeling

Jonas B. Ruh, Valentí Sallarès, César R. Ranero, Taras Gerya

AGU PUBLICATIONS

JGR

Journal of Geophysical Research: Solid Earth

RESEARCH ARTICLE
10.1002/2016JB013250

Key Points:
- We investigate brittle deformation and stress evolution in overriding plates during seamount indentation
- Underthrusting seamounts strongly fracture upper plate; topographic effects diminish with ongoing descendence
- Seamount subduction induces a typical stress pattern with large tectonic overpressure and underpressure above the flanks of the seamount

Correspondence to:
J. B. Ruh,
jruh@ictja.csic.es

Citation:
Ruh, J. B., V. Sallarès, C. R. Ranero, and T. Gerya (2016), Crustal deformation dynamics and stress evolution during seamount subduction: High-resolution 3-D numerical modeling, *J. Geophys. Res. Solid Earth*, *121*, 6880–6902, doi:10.1002/2016JB013250.

Received 3 JUN 2016
Accepted 28 AUG 2016
Accepted article online 31 AUG 2016
Published online 17 SEP 2016

Crustal deformation dynamics and stress evolution during seamount subduction: High-resolution 3-D numerical modeling

Jonas B. Ruh[1,2], Valentí Sallarès[3], César R. Ranero[3], and Taras Gerya[4]

[1]Institut des Sciences de la Terre de Paris, Université Pierre et Marie Curie, Paris, France, [2]Institut de Ciències de la Terra Jaume Almera, Consejo Superior de Investigaciones Cientificas, Barcelona, Spain, [3]Institut de Ciències del Mar, Consejo Superior de Investigaciones Cientificas, Barcelona, Spain, [4]Institute of Geophysics, Department of Earth Sciences, ETH Zurich, Zurich, Switzerland

Abstract Seamounts or submarine volcanoes frequently collide with the overriding crust along presently active subduction zones locally modifying stress and permanent deformation patterns. Dynamics of this process is not fully understood, and several end-member scenarios of seamount-crust interaction are proposed. Here we use high-resolution 3-D numerical models to investigate evolution of crustal deformation and stress distribution within the upper plate induced by the underthrusting of subducting seamounts. The dynamical effects of the upper plate strength, subduction interface strength, and strain weakening of the crust are investigated. Experiment results demonstrate that characteristic crustal fracturing patterns formed in response to different seamount-crust interaction scenarios. Indenting seamounts strongly deform the overriding plate along a corridor as wide as the underthrusting seamount by constantly shifting subvertical shear zones rooted at the seamount extensions. A reentrant develops during initial seamount collision. A topographic bulge atop the seamount and lateral ridges emerge from further seamount subduction. Obtained stress pattern shows areas of large overpressure above the rearward and large underpressure above the trenchward flank of the seamount. Results of numerical experiments are consistent with seismic reflection images and seismic velocity models of the upper plate in areas of seamount subduction along the Middle America Trench and give important insights into the long-lasting question, whether subducting seamounts and rough seafloor act as barriers or asperities for megathrust earthquakes.

1. Introduction

Oceanic plates contain a vast amount of seamounts that are either scattered or form linear chains [*Hillier and Watts*, 2007; *Smith and Jordan*, 1988]. Those seamounts have very different dimensions, from hundreds of meters to several kilometers tall and few to over a hundred kilometers wide. They migrate within the ocean plates toward subduction trenches according to plate motion and eventually collide with continental margins where oceanic plates subduct [*von Huene*, 2008]. Collision of seamounts with overriding plates at trenches has been studied worldwide along many trenches [e.g., *Bangs et al*., 2006; *Collot and Fisher*, 1989; *Timm et al*., 2013; *von Huene et al*., 1997].

Seamounts initially collide with the toe of the margin and later tunnel beneath the thickening continental wedge [*Ranero and von Huene*, 2000]. The overriding plate displays characteristic topographic features due to this process including seafloor embayments, a bulge above underthrusting seamounts, collapsing slope material in the wake of the seamounts, and a resulting furrow delineating the seamount subduction path [*Lallemand and Le Pichon*, 1987; *Ranero and von Huene*, 2000; *Ruh*, 2016]. Regarding the dynamic evolution of the continental margin wedge down to the subduction interface, *Wang and Bilek* [2014] summarized three potential end-member scenarios for the mechanical response during seamount subduction partially based on earlier published studies (Figure 1): (i) *Cloos* [1992] and *Cloos and Shreve* [1996] proposed that seamounts can be cut off entirely within the subduction channel shear zone, (ii) *Scholz and Small* [1997] suggested that the continental wedge slides without major internal deformation over the subducting seamount, and (iii) *Wang and Bilek* [2011] indicated the possibility of seamounts breaking through the continental wedge by severely fracturing its surrounding.

The above listed scenarios have been used to relate seamount subduction and megathrust seismicity. *Cloos and Shreve* [1996] argue that in Chilean-type subduction zones, where subducting sediment thins by compaction in the subduction channel below the continent, large earthquakes might occur where seamounts hit the

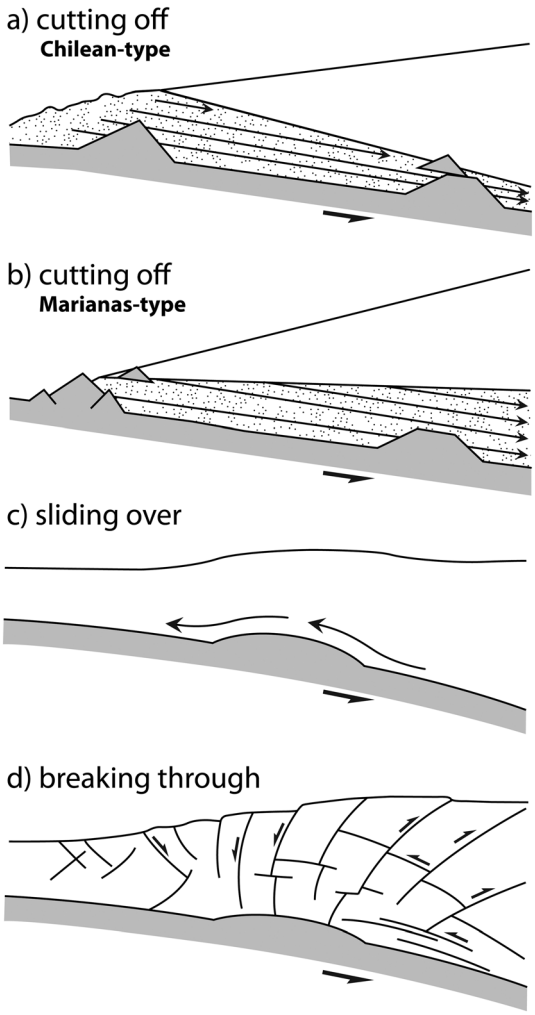

Figure 1. Suggested scenarios of overriding plate response to subduction of a seamount (adapted from *Wang and Bilek* [2014]). Figures 1a and 1b show cutting off of subducting seamounts according to *Cloos and Shreve* [1996]: (a) Large earthquakes occur due to seamount decapitation at high confining pressures. (b) Absence of large earthquakes due to very shallow seamount decapitation. (c) The upper plate slides over subducting seamounts without internal deformation [*Scholz and Small*, 1997]. Resulting bending stresses potentially increase normal stress on the plate interface. (d) Subducting seamount severely breaks, i.e., fractures the overriding plate [*Wang and Bilek*, 2011]. Heterogeneous fracture network reduces interpolate coupling.

overriding rigid block (Figure 1a). In Marianas-type erosional subduction zones, seamounts might be truncated at shallow level (low confining pressure) but subduct aseismically at greater depth (Figure 1b). *Scholz and Small* [1997] propose that the elastic flexure of the overriding plate sliding over a subducting seamount leads to locally increased normal stresses on the subduction interface, enhancing seismic coupling (Figure 1c). This would imply that the overriding plate deforms purely elastically because brittle faults would release accumulated flexural elastic strain, i.e., stresses. Contrariwise, *Wang and Bilek* [2011] postulated that the permanent brittle deformation of the overriding plate induced by seamount subduction develops a complex heterogeneous stress field which does not support the generation of large earthquakes but rather an environment favorable for aseismic creep (Figure 1d). Although field observations support that seamounts are related to seismic initiation and rupture propagation arrest, the actual relation between seamount subduction and megathrust seismicity is a matter of debate [e.g., *Geersen et al*., 2015; *Kodaira et al*., 2000; *Mochizuki et al*., 2008; *Watts et al*., 2010]. It has been proposed that subduction of rough seafloor rather limits than favors the occurrence of very large earthquakes [*Wang and Bilek*, 2014].

To what extend the overriding plate and the seamount itself are deforming and how stresses are reorganized during collision is not fully understood. Surface topography above subducted seamounts and seismic imaging indicate that most seamounts survive to depths of 20–30 km [e.g., *von Huene et al*., 2000], whereas complete decapitation of seamounts at crustal levels is rare [*Wang and Bilek*, 2014, and references therein]. On the other hand, exhumed pieces of subducted seamounts in Japan indicate that seamounts are dismembered into fragments 1 to 2 orders of magnitude smaller than their initial size [*Isozaki et al*., 1990] or underplated and stacked as coherent units at depths of 20–30 km [*Ueda*, 2005]. However, these structures—inferred from the fossil record—are inadequately documented worldwide and could represent exceptional events during seamount subduction.

Analogue models have reproduced a dense network of faults within the overriding plate caused by subducting seamounts [*Dominguez et al*., 2000; *Dominguez et al*., 1998b; *Lallemand et al*., 1992] and elongated ridges [*Hampel et al*., 2004]. The resemblance of surface morphology between sandbox models and natural examples obtained with seafloor mapping tools suggests that the observed style of upper plate deformation

occurs at convergent margins where large seamounts subduct [*Dominguez et al*., 1998b]. However, little has been attempted so far to analyze with numerical models the complex stress field within and around a subducting seamount [*Ruh*, 2016; *Zeumann and Hampel*, 2015]. Dynamic earthquake rupture models infer that subducting seamounts may have a strong effect on the evolution of seismic events, acting either as a barrier or as an area of large stress drop [*Duan*, 2012; *Yang et al*., 2012, 2013]. As argued by *Wang and Bilek* [2014], these models ignore the effect of the seamount as a geometrical irregularity but implement it as a patch of increased normal stress on the planar fault, an assumption that is not necessarily correct. *Baba et al*. [2001] reproduced the incremental stress field associated with seamount subduction by applying continuum numerical simulations with a purely elastic rheology. Results manifest a concentration of increased shear stresses along the flanks of the seamount. However, over longer time scales, the rheology of a continental margin is rather characterized as a Coulomb material than as purely elastic [*Lallemand et al*., 1994]. Therefore, a more complex crustal rheology model is needed to simulate the generation and evolution of a complex fracture system and the resulting absolute stress field.

Here we present 3-D high-resolution dynamic numerical experiments of seamounts colliding perpendicular with a continental margin. The impact of oblique subduction of seafloor irregularities has yet been studied with numerical and analogue modeling techniques [*Dominguez et al*., 1998a; *Hampel et al*., 2004; *Zeumann and Hampel*, 2015]. The applied numerical code includes a brittle/plastic rheology and is therefore able to reproduce an expected complex fracture network observed in analogue models and seafloor maps [e.g., *Dominguez et al*., 1998b; *Wang and Bilek*, 2011]. Our aim is to understand the expression of permanent deformation and the evolution of the stress field within the continental crust during seamount underthrusting depending on upper plate strength. Furthermore, the topographic morphology obtained by our models is compared to natural examples of the Middle America Trench.

2. Numerical Model

The numerical code I3ELVIS used for the modeling of seamount subduction is based on a combination of a finite difference method, applied on a staggered Eulerian grid, and a marker-in-cell technique (I3ELVIS) [*Gerya*, 2010; *Gerya and Yuen*, 2007]. The momentum and mass conservation equations are solved on the Eulerian frame, and physical properties are transported by Lagrangian markers that move according to the velocity field interpolated from the fixed grid. Non-Newtonian viscous-brittle/plastic rheologies are used in the model. Governing equations and the numerical implementation are described in Appendix A.

The Eulerian computational domain has dimensions of 97.2 · 49.2 · 22.2 km (Figure 2a) and is resolved with a regular rectangular grid of 325 · 165 · 149 nodes and contains ~63 million randomly distributed Lagrangian markers. The initial model geometry is set up to resemble the continental margin offshore NW Costa Rica and Nicaragua [*Ranero et al*., 2008, Figure 2] away from Cocos Ridge. It contains a 450 m thick lowermost rigid subducting plate underlaying a 450 m thick décollement/subduction interface (450 m = thickness of three Eulerian cells for accurate resolution). Above, the continental margin section is prescribed, which thins out toward the trench (Figure 2a). A 300 m thick sedimentary sequence covers the incoming oceanic plate. The oceanic plate contains a conical seamount (base radius = 9.14 km, peak height = 2.45 km, and flanks slope = 15°) cutting through décollement and sediments (Figure 2a). Free surface condition is implemented by using a low-viscosity (10^{18} Pa s), low-density (1 kg/m^3) "sticky air" filling the rest of the computational domain [e.g., *Schmeling et al*., 2008].

At the bottom, a constant velocity boundary condition with $v_x = -1$ cm/yr is applied to prescribe the subducting plate motion. New oceanic plate material is supplied through the right boundary. Free slip boundary condition is used at the frontal and rear sides and at the top of the model. Dip angle of the subducting plate corresponds to 10°, which is prescribed by using an inclined gravitational acceleration vector $g = 9.81$ m/s^2 ($g_x = 1.7$ m/s^2, $g_y = 0$, and $g_z = 9.66$ m/s^2; Figure 2a). The initial margin geometry thus has a flat shelf ($\alpha = 0°$) from 0 to 30 km in x direction and a slope area ($\alpha = 5°$) between 30 and 80 km (Figure 2a).

Constant density $\rho = 2800$ kg/m^3 is used for all rock types. The basal rigid plate has a fixed viscosity of $\eta_{\text{rigid plate}} = 10^{23}$ Pa s, which does not change during the simulation. Other rock types have constant viscosity of $\eta_{\text{rock}} = 10^{23}$ Pa s, which is combined with a brittle/plastic rheology. Brittle/plastic failure criterion is defined

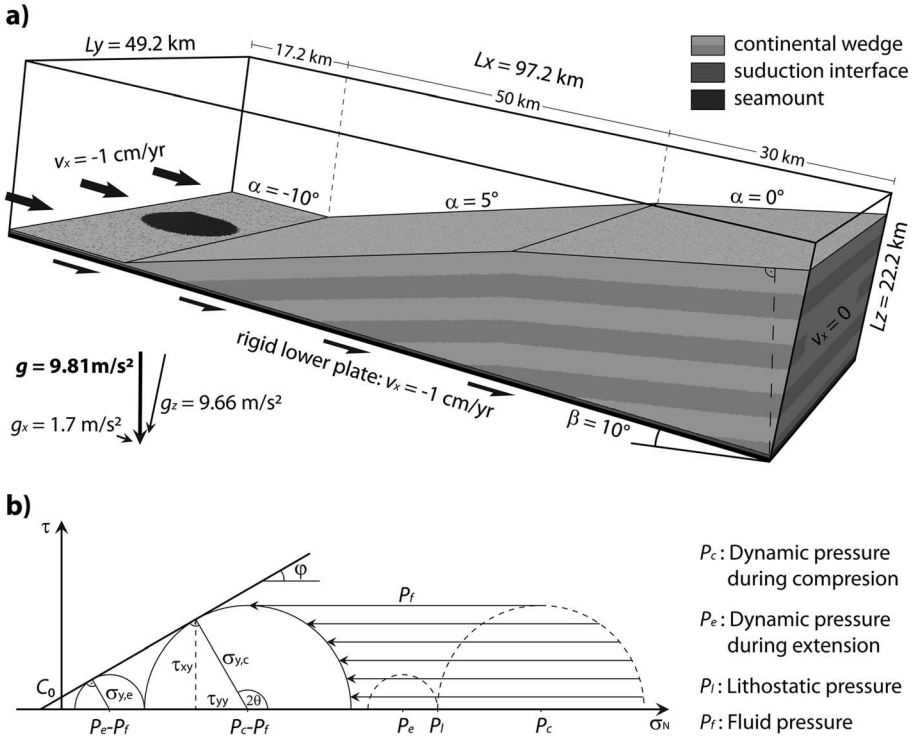

Figure 2. (a) Geometrical model setup. Eulerian grid box is rotated 10° around *y* axis defined by gravitational acceleration in *x* and *z* directions. Overriding plate (grey) is defined by 30 km of horizontal shelf and a 50 km wide slope with an angle of 5°. Incoming seamount is located at the left (black). (b) Mohr circle defining brittle strength depending on fluid pressure P_f and tectonic process (extensional versus contractional) in two dimensions. Dynamic pressure deviates from lithostatic pressure (minus fluid pressure) by the Drucker-Prager yield stress σ_y.

by the Drucker-Prager formulation depending on dynamic pressure P, friction angle ϕ, cohesion C_0, and fluid pressure ratio λ:

$$\sigma_y = P(1-\lambda)\cdot\sin\phi + C_0\cdot\cos\phi \tag{1}$$

where

$$\lambda = \frac{P_{\text{fluid}}}{P_{\text{dynamic}}}. \tag{2}$$

In two dimensions, this yield criterion can be illustrated on a Mohr circle (Figure 2b) with

$$\sigma_y = \sqrt{\frac{1}{2}\tau_{ij}^2}. \tag{3}$$

Having in mind that $P_{\text{dynamic}} = g\cdot\rho\cdot h + \sigma_y$ in compression and $P_{\text{dynamic}} = g\cdot\rho\cdot h - \sigma_y$ in extension, where g is gravitational acceleration, ρ density, and h depth, deviation of dynamic pressure from lithostatic pressure (deviatoric stress) during brittle failure in 2-D can be described as

$$\sigma'_{\text{comp}} = \frac{\sin\phi\cdot g\cdot\rho\cdot h\cdot(1-\lambda) + \cos\phi\cdot C_0}{1-\sin\phi\cdot(1-\lambda)} \tag{4}$$

and

$$\sigma'_{\text{ext}} = \frac{\sin\phi\cdot g\cdot\rho\cdot h\cdot(1-\lambda) + \cos\phi\cdot C_0}{1+\sin\phi\cdot(1-\lambda)}. \tag{5}$$

In three dimensions, these values can differ due to additional shear stresses.

2.1. Brittle/Plastic Strength of Upper Plate and Subduction Interface

All modeled rocks (continental margin, sediments, interface, and seamount) have an internal friction angle of $\phi = 30°$ [*Byerlee*, 1978]. Cohesion amounts $C_0 = 10$ MPa for continent and sediments, $C_0 = 5$ MPa for the

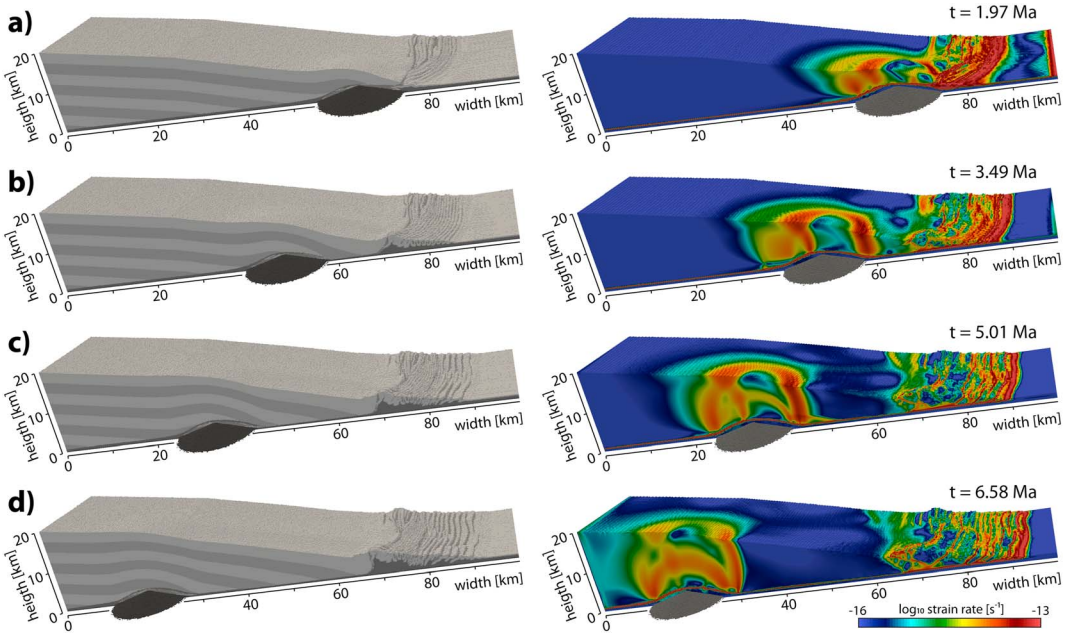

Figure 3. Temporal evolution of the reference model cut at *Ly*/2. Complete seamount is illustrated. Lower plate is pulled out toward the left. (a) At 1.97 Ma, (b) at 3.49 Ma, (c) at 5.01 Ma, and (d) at 6.58 Ma. Composition showing upper plate in grey colors and seamount in black (left). Closure of reentrant at deformation front between 2 and 4 Ma. Second invariant of the strain-rate tensor indicates characteristic fracturing pattern due to seamount indentation and continuing deformation of the frontal prism (right).

subduction interface, and $C_0 = 20$ MPa for the seamount. Strength differences of the overriding plate and the subduction interface are defined by their fluid pressure ratio (equations (1) and (2)). Seismic imaging reveals that free fluids accumulate along the plate interfaces at subduction zones [e.g., *Bangs et al.*, 2015; *Ranero et al.*, 2008]. The source of those fluids is mainly a result of dehydration of smectite and biogenic opal between ~50 and 160°C [*Spinelli and Underwood*, 2004]. This is supported by an increased density of fluid seep occurrence above the plate boundary with respective temperatures [*Ranero et al.*, 2008]. Furthermore, fluid seeps along nonaccretionary margins indicate that fluids mainly migrate upward from the plate interface into the continental crust. Fluid flow measurements and chemical modeling of these fluids indeed suggest that less than 10% of the deep expelled fluids migrate laterally along the plate boundary toward the trench [*Hensen and Wallmann*, 2005; *Ranero et al.*, 2008].

Fluid pressures in a saturated medium can range from hydrostatic to dynamic pressure. To cover a large spectrum of potential apparent fluid pressures within the overriding crust, applied values for $\lambda_{\text{upper plate}}$ in our experiments are 0.36 (hydrostatic for $\rho_{\text{upper plate}} = 2800\,\text{kg/m}^3$ and $\rho_{\text{fluid}} = 1000\,\text{kg/m}^3$ in the absence of any tectonic overpressure), 0.63, and 0.9. These values for fluid pressure ratio cover the interval analyzed for different margins worldwide [*Cubas et al.*, 2013; *Davis et al.*, 1983; *Wang and Hu*, 2006]. Fluid pressures along the subduction interface are suggested to be highly elevated. Estimated values for λ calculated from V_p/V_s ratios range from 0.94 to 0.98 [*Moreno et al.*, 2014]. Force balancing of topographic loading provides $\lambda \approx 0.95$ as a long-term average value along plate interfaces [*Lamb*, 2006]. Fluid pressure ratios of the plate interface applied here in experiments are $\lambda_{\text{interface}} = 0.92$, 0.95, and 0.98.

To test the influence of elevated fluid pressures along spontaneously forming fracture zones within the upper plate [*Dymkova and Gerya*, 2013], additional experiments including plastic strain weakening are presented. Sediments and seamounts are linearly weakened by increasing fluid pressure according to

$$\lambda_{\text{weakened}} = \frac{\lambda_{\text{upper plate}} + 1}{2} \tag{6}$$

and lowering C_0 to 0.2 MPa according to accumulated plastic strain ε_{pl} between $0 < \varepsilon_{\text{pl}} < 1$ [*Ruh et al.*, 2014].

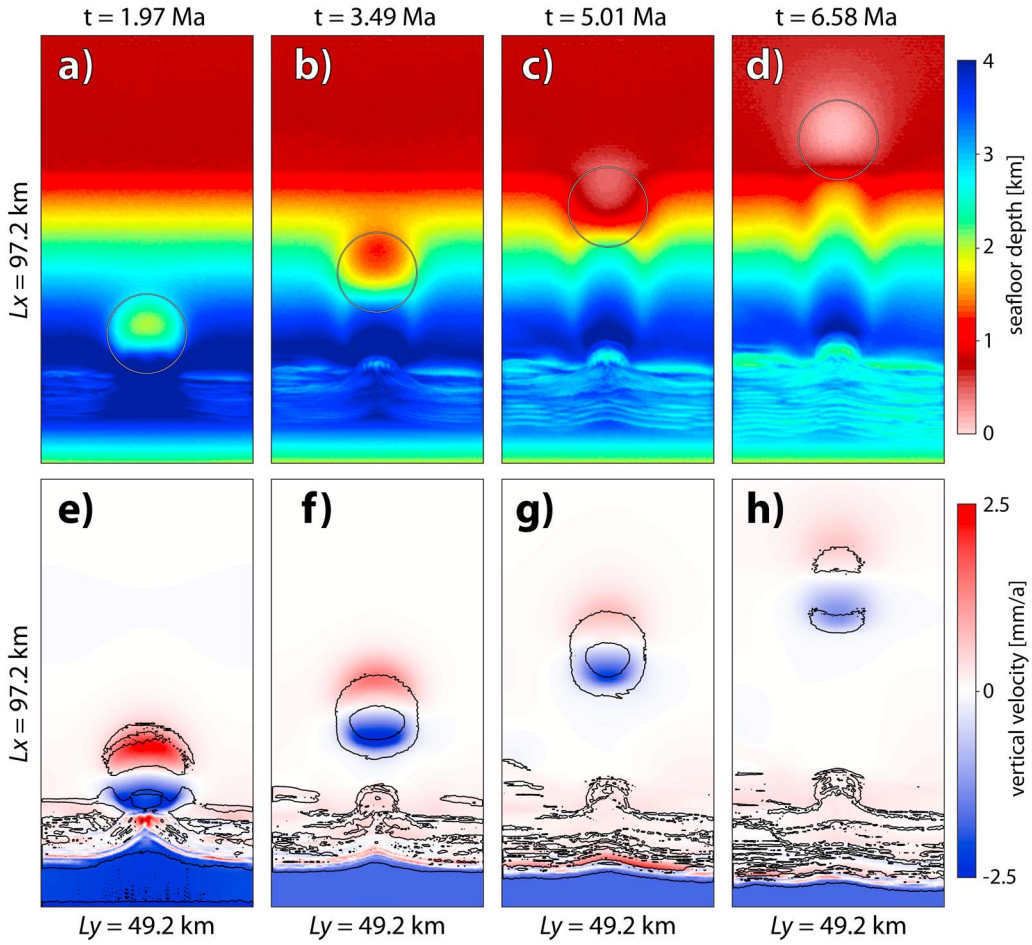

Figure 4. Topographic evolution of the reference model in map view. (a) At 1.97 Ma, (b) at 3.49 Ma, (c) at 5.01 Ma, and (d) at 6.58 Ma. Figures 4a–4d show seafloor depth assuming a 300 m deep horizontal shelf (see Figure 2). Circle indicates the base of the seamount. Topographic expression atop the seamount decreases with ongoing seamount subduction. (e–h) Vertical velocities at the surface of the overriding plate. Contours indicate strain rate of $\dot{\varepsilon} = 5 \cdot 10^{-15}\ s^{-1}$. Vertical surface velocities decrease with descending seamount.

3. Results

We conducted eight numerical simulations for various values of fluid pressure ratio λ (and therefore varying brittle strength) of the subduction interface and the overriding plate. In addition, three experiments were run to evaluate the effects of strain weakening.

3.1. Dynamics of Seamount Indentation

Figure 3 shows the evolution of our reference model with intermediate interface and overriding plate strength ($\lambda_{\text{interface}} = 0.95$; $\lambda_{\text{upper plate}} = 0.63$). Both lithological structure markers and the second invariant of the strain-rate tensor record deformation within the upper continental plate, with areas of fast deformation indicated by localization of high brittle/plastic strain rates (Figure 3). After 1.97 Ma, the whole seamount has been thrusted under the overriding plate. Accretion of the frontal sediment prism is accompanied by high strain-rate values along the trench (Figure 3a). The curved outline of this high strain-rate zone, i.e., the margin toe, also visible in the lithological structure, is the result of stalled frontal accretion during seamount collision at the trench and forms a so-called reentrant. Frontal accretion of the thin incoming sediment layer commences again when the overriding plate has completely overthrust the incoming seamount. At 3.49 Ma, the deformation front is sublinear over the whole model width and the reentrant has been closed (Figure 3b). A high strain-rate horizon separating the downgoing slab and seamount from the overriding plate corresponds to the active subduction interface.

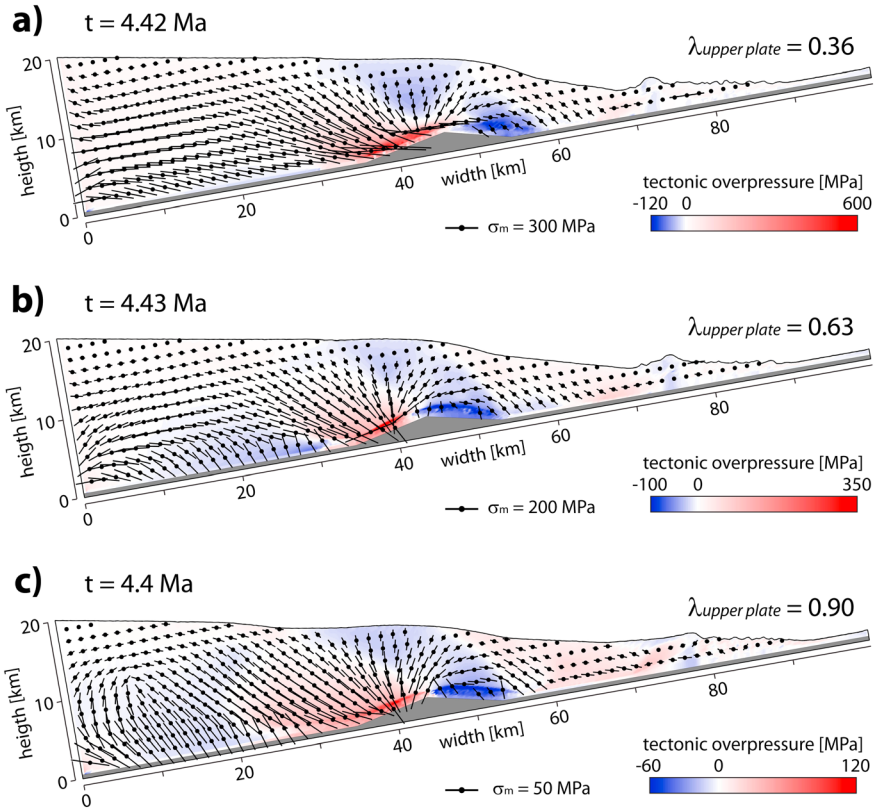

Figure 5. Cross sections at *Ly*/2 of tectonic overpressure and underpressure (deviation from lithostatic pressure) for simulations with different upper plate strength and equal subduction interface strength ($\lambda_{interface} = 0.95$) at 4.4 Ma. Rigid lower plate and seamount in grey. (a) $\lambda_{upper\ plate} = 0.36$. (b) $\lambda_{upper\ plate} = 0.63$. (c) $\lambda_{upper\ plate} = 0.9$. Values of tectonic pressure deviation decrease with decreasing upper plate strength. Patterns of dynamic pressure and principal stress orientation are similar. Large overpressure and underpressure at the seamount flanks. Compression along the wedge toe, extension close to the rear.

Within the overriding plate, high strain rate localizes subvertically above the seamount tip and at the trenchward outline of the seamount. In map view, the increased strain-rate zone takes on a circular shape (Figure 3b). After 5.01 Ma, the deformation zone above the seamount exhibits three subvertical zones of increased strain rate and is clearly separated from the frontal accretion of sediments (Figure 3c). The three strongly localized strain-rate zones are located above the frontal edge, the apex, and the shallower edge of the seamount. A further zone of strain-rate localization forms a curved band over the seamount, merging with the middle subvertical shear zone. The subvertical shear zones rooting at the lower edge and the apex join upward near the seafloor, where they form a ring-like structure together with the subvertical shear zone above the shallow edge of the seamount (Figure 3c). The subduction interface smoothly overrides the subducting seamount to reach the deformation front at ~90 km (*x* axis). During further subduction of the seamount, maximal values and localization on the subvertical high strain-rate shear zones decrease (Figure 3d). On the other hand, deformation along the curved shear zone roughly parallel to the seamount top becomes predominant. In summary, localized high-strain-rate shear zones indicate an evolving spatial distribution of brittle deformation in the upper plate as the seamount subducts. Due to the motion of the seamount with respect to the overriding plate, shear bands are not locally active long enough to develop fault zones with observable offsets in plots of the compositional markers, although the upward bending of the upper plate is accompanied by brittle deformation (Figure 3).

The modeled topographic evolution and vertical movement of the seafloor caused by seamount underthrusting are shown in Figure 4. At 1.97 Ma, a low-topographic reentrant at the margin toe can be observed with a width equal to the base of the seamount (~20 km). The bulge atop of the underthrusting seamount is a ~20 km wide and ~2 km high with respect to the surrounding topography (Figure 4a). After 3.49 Ma, lateral ridges parallel to the convergence vector develop, delineating a furrow in the wake of the

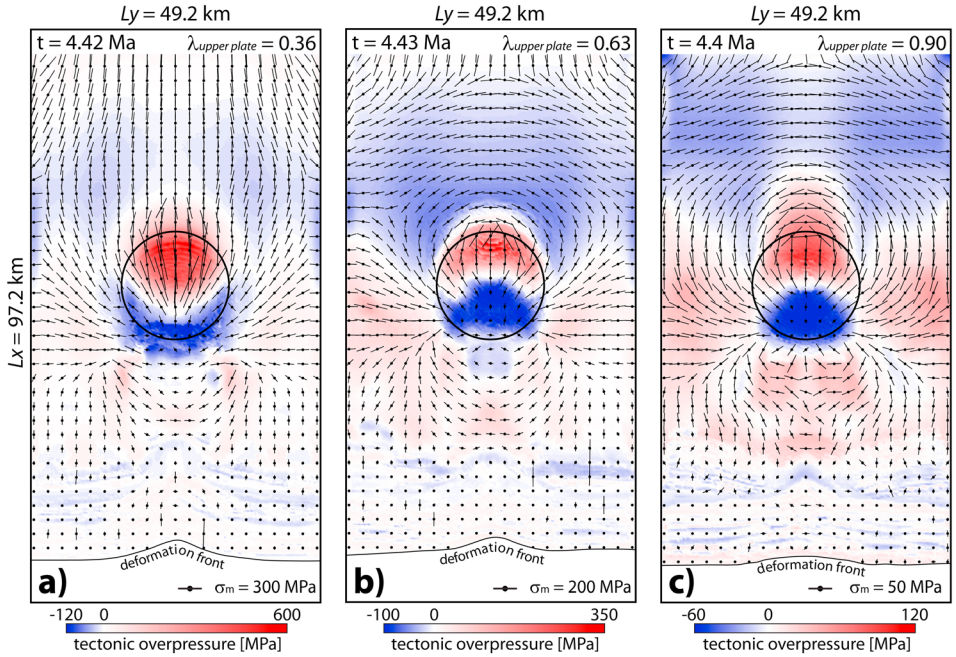

Figure 6. Tectonic overpressure and underpressure (deviation from lithostatic pressure) at the bottom of the overriding plate for simulations with different upper plate strength and equal subduction interface strength ($\lambda_{\text{interface}} = 0.95$) at 4.4 Ma. (a) $\lambda_{\text{upper plate}} = 0.36$. (b) $\lambda_{\text{upper plate}} = 0.63$. (c) $\lambda_{\text{upper plate}} = 0.9$. Values of tectonic pressure deviation decrease with decreasing upper plate strength. Sizes of large overpressure and underpressure patches are roughly delimited by the seamount extent (black circle).

subducting seamount (Figure 4b). The topographic expression of the bulge decreases with ongoing seamount subduction. After 6.58 Ma, the bulge above the seamount has a height of ~500 m, with respect to its surrounding topography (Figure 4d).

At an early stage of seamount subduction, vertical velocities at the seafloor are ~2.5 mm/a above the rearward side of the seamount and ~ –2.5 mm/a above the trenchward side (Figure 4e). Subsequently, the vertical movement at the seafloor diminishes to ±1 mm at 6.58 Ma during ongoing seamount subduction (Figures 4e–4h). Additionally, black lines indicating the strain-rate contour at $\dot{\varepsilon} = 5 \cdot 10^{-15}\,\text{s}^{-1}$ illustrate a decreasing surface area of elevated strain rates ($\dot{\varepsilon} > 5 \cdot 10^{-15}\,\text{s}^{-1}$), as observed in Figure 3.

3.2. Stresses in the Overriding Plate During Seamount Subduction

The stress and pressure states of experiments after ~4.4 Ma are illustrated by plots of the largest principal stresses and the divergence of dynamic pressure from lithostatic pressure, hereafter named tectonic underpressure and overpressure [*Mancktelow*, 1995; *Petrini and Podladchikov*, 2000]. Vertical profiles of the *x-z* plane cut at $y = Ly/2$ (Figures 5 and 7), whereas horizontal profiles show the dynamic pressure in the overriding plate 500 m above the interface (Figures 6 and 8). The largest principal stress, σ_m, is plotted with direction and dimension on top of the dynamic pressure cross sections.

3.2.1. Influence of Overriding Plate Strength

The effect of upper plate strength on stress distribution is illustrated based on experiments with equal interface strength ($\lambda_{\text{interface}} = 0.95$) but different fluid pressure ratios within the overriding plate ($\lambda_{\text{upper plate}} = 0.36$, 0.63, and 0.9). Vertical cross sections at $y = Ly/2$ show that the largest overpressure occurs above the rearward (i.e., leading) flank of the subducting seamounts in all experiments (Figure 5). In areas of compression, σ_m are oriented toward the seamount. Areas of comparatively larger underpressure are located above the trenchward flank of the seamount. All three simulations, furthermore, exhibit a triangular zone of tectonic underpressure between ~5 km above the seamount apex that extends up to the seafloor, indicating an area that is undergoing extension. Absolute values for underpressure and overpressure decrease with increasing fluid pressure ratio (Figure 5), where tectonic pressures that can develop will be limited by the strength of the confining upper plate [*Mancktelow*, 1995, 2008].

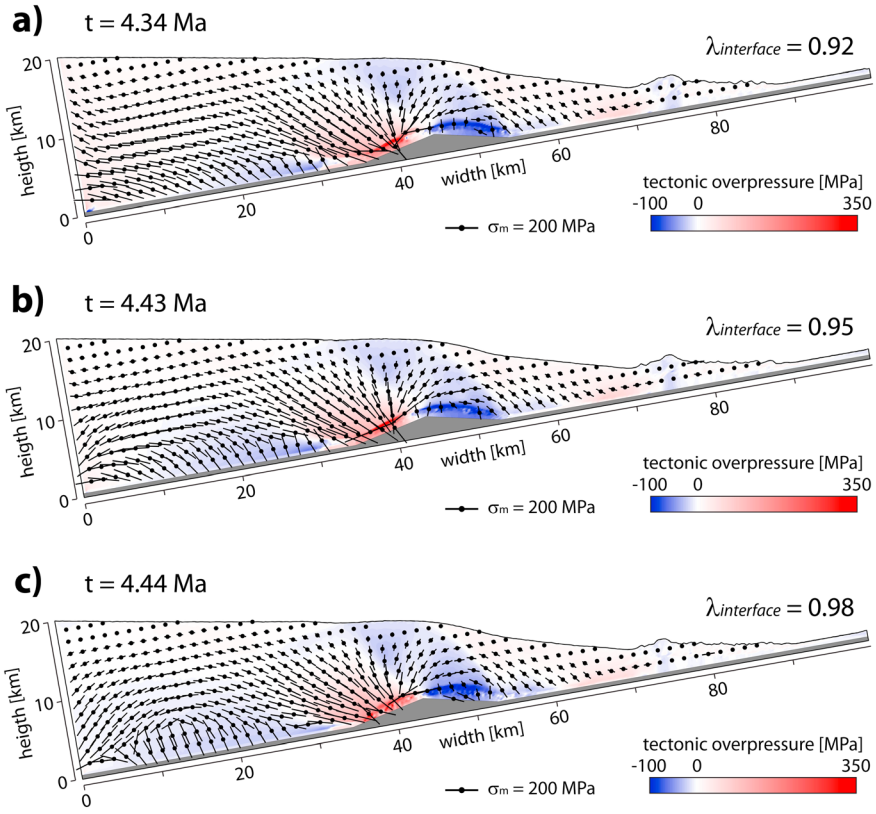

Figure 7. Cross sections at *Ly*/2 of tectonic overpressure and underpressure (deviation from lithostatic pressure) for simulations with different subduction interplate strength and upper plate strength ($\lambda_{\text{upper plate}} = 0.63$) at 4.4 Ma. Rigid lower plate and seamount in grey. (a) $\lambda_{\text{interface}} = 0.92$. (b) $\lambda_{\text{interface}} = 0.95$. (c) $\lambda_{\text{interface}} = 0.98$. Values and patterns of dynamic pressure and principal stress orientation are similar. Large overpressure and underpressure at the seamount flanks. Compression along the wedge toe, extension close to the rear.

Stress regimes in the upper plate ahead of the seamount ($x = 0$–30 km) differ depending on overriding plate strength: (i) For $\lambda_{\text{upper plate}} = 0.36$, the upper plate is overpressured with near-horizontal orientation of σ_m, indicating a compressional stress state (Figure 5a). (ii) For $\lambda_{\text{upper plate}} = 0.63$, the lowermost ~5 km of the upper plate is under extensional stresses, illustrated by local underpressure and near-vertical σ_m (Figure 5b). (iii) For fluid pressures close to tectonic pressure ($\lambda_{\text{upper plate}} = 0.9$), a large area of the upper plate ($x = 0$–25 km and $z = 0$–12 km) is under an extensional stress field (Figure 5c). All experiments show compressional stresses and corresponding tectonic overpressure trenchward of the seamount ($x > 60$ km).

Profiles 500 m above the subduction interface show that the areas of largest overpressure and underpressure are delimited by the vertical projection of the seamount outline, with overpressure above the leading flank of the seamount and underpressure above the trenchward flank (Figure 6). Furthermore, away from the seamount, the base of the upper plate of the experiment with $\lambda_{\text{upper plate}} = 0.36$ is mainly under compression, except for two small patches ahead of the seamount (Figure 6a). For larger fluid pressure ratios ($\lambda_{\text{upper plate}} = 0.63$ and 0.9), stresses in the upper plate ahead of the seamount are extensional, whereas trenchward they are mainly compressional (Figures 6b and 6c). Along these presented profiles, absolute values for underpressure and overpressure decrease with increasing fluid pressure ratio.

Orientation of the principal stress σ_m is generally parallel to the *x* axis for compressional field (Figure 6a) and near parallel to the *y* axis for extensional fields (Figures 6b and 6c). On top of the leading seamount flank, the experiments show stress orientations parallel to the movement direction of the seamount. At the side of seamounts and on their trenchward flanks, principal stresses rotate toward the wake, which is the underpressured region (Figure 6).

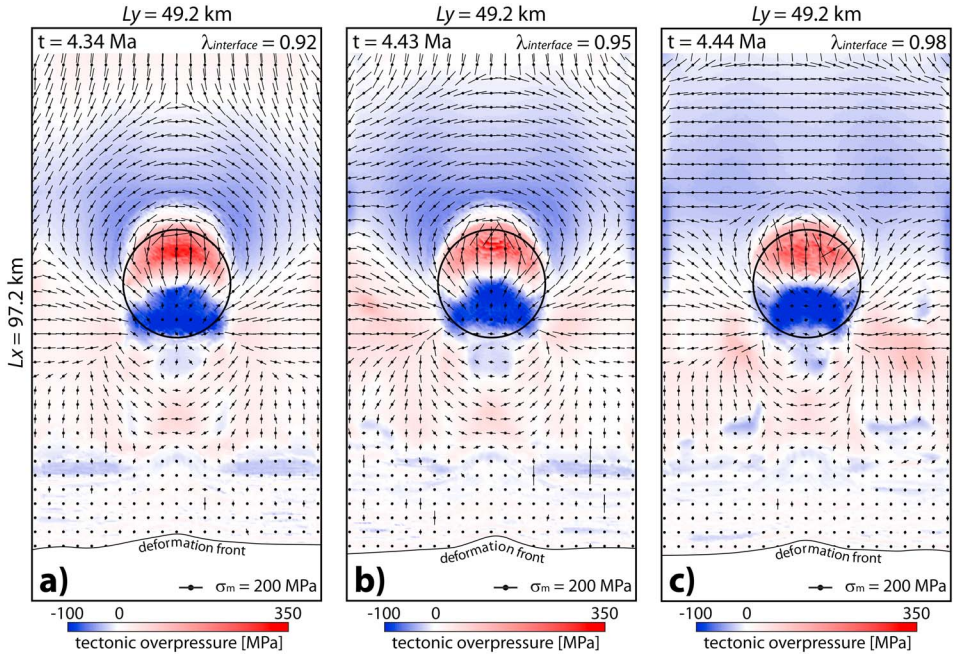

Figure 8. Tectonic overpressure and underpressure (deviation from lithostatic pressure) at the bottom of the overriding plate for simulations with different subduction interface strength and equal upper plate strength ($\lambda_{\text{upper plate}} = 0.63$) at 4.4 Ma. (a) $\lambda_{\text{interface}} = 0.92$. (b) $\lambda_{\text{interface}} = 0.95$. (c) $\lambda_{\text{interface}} = 0.98$. Values of tectonic pressure deviation are independent of interface strength. Sizes of large overpressure and underpressure patches are roughly delimited by the seamount extent (black circle).

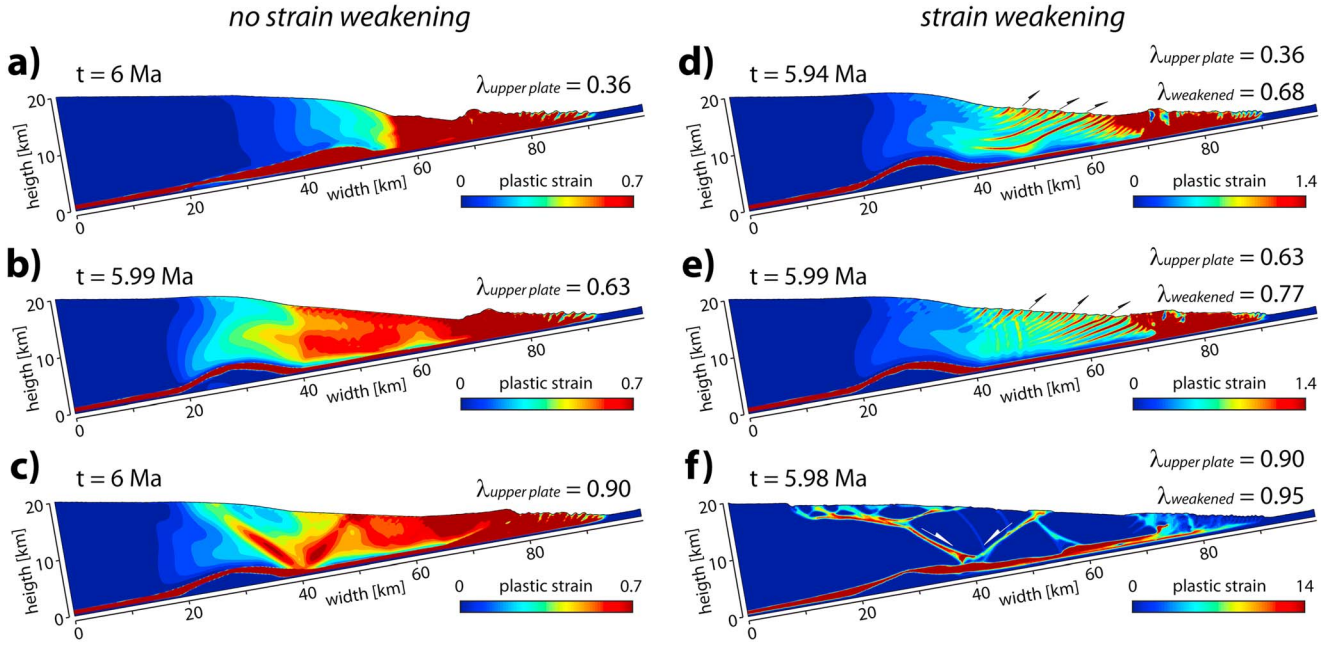

Figure 9. Cross sections at $Ly/2$ of accumulated plastic strain for simulations with different upper plate strength at 6 Ma. (a–c) No strain weakening. (d–f) Strain weakening (double of the initial fluid pressure at plastic strain $\varepsilon_{\text{pl}} = 1$). $\lambda_{\text{upper plate}} = 0.36$ (Figures 9a and 9d). $\lambda_{\text{upper plate}} = 0.63$ (Figures 9b and 9e). $\lambda_{\text{upper plate}} = 0.9$ (Figures 9c and 9f). Seamount gets only deformed for $\lambda_{\text{upper plate}} = 0.36$ and without strain weakening (Figure 9a). Large-scale normal faults (white arrows) develop for very weak upper plates (Figures 9c and 9f). Black arrows indicate thrust shear zones in the wake of seamounts (Figures 9d and 9e).

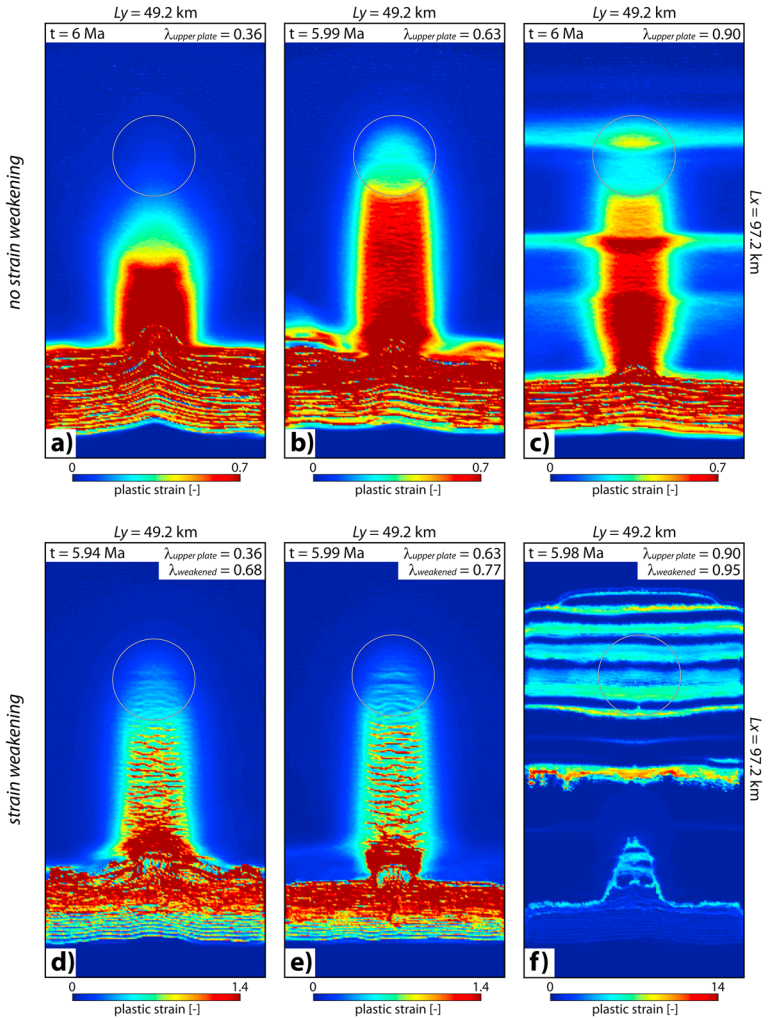

Figure 10. Map view of accumulated plastic strain at the surface for simulations with different upper plate strength at 6 Ma. Circle: seamount location. (a–c) No strain weakening. (d–f) Strain weakening (double of the initial fluid pressure at plastic strain $\varepsilon_{pl} = 1$). $\lambda_{upper\ plate} = 0.36$ (Figures 10a and 10d). $\lambda_{upper\ plate} = 0.63$ (Figures 10b and 10e). $\lambda_{upper\ plate} = 0.9$ (Figures 10c and 10f). Seamount gets only deformed for $\lambda_{upper\ plate} = 0.36$ and without strain weakening (Figure 10a). Overriding plate deformation is strongly influenced by seamount indentation, where the deformation scar is equally wide as the seamount. Large-scale normal faults develop for very weak upper plates (Figures 10c and 10f).

3.2.2. Influence of Subduction Interface Strength

The effect of subduction interface strength on stress distribution is illustrated by experiments with equal upper plate strength ($\lambda_{upper\ plate} = 0.63$) but different fluid pressure ratios along the interface ($\lambda_{interface} = 0.92$, 0.95, and 0.98). Vertical profiles at $y = Ly/2$ show that regions of large overpressure and underpressure occur on the flanks of the seamount for all experiments, where absolute values for underpressure and overpressure do not differ significantly for different interface strengths (Figure 7).

σ_m above the leading flank of the seamount are oriented toward the seamount peak, independent of the interface strength. Furthermore, the top ~10 km of the rearward part of the continental margins ($x < 30$ km) are generally under compression, showing near-horizontal principal stresses σ_m (Figure 7). However, for $\lambda_{interface} = 0.92$, the bottom of the overriding plate between $x = 20$ and 30 km is underpressured, with a near-vertical orientation of σ_m (Figure 7a). This underpressured area landward of the seamount increases for experiments with increasing interface fluid pressure ratios (Figures 7b and 7c).

Slices 500 m above the subduction interface show the largest overpressure and underpressure delimited by the outline of the seamount base (Figure 8). Furthermore, absolute values for underpressure and overpressure

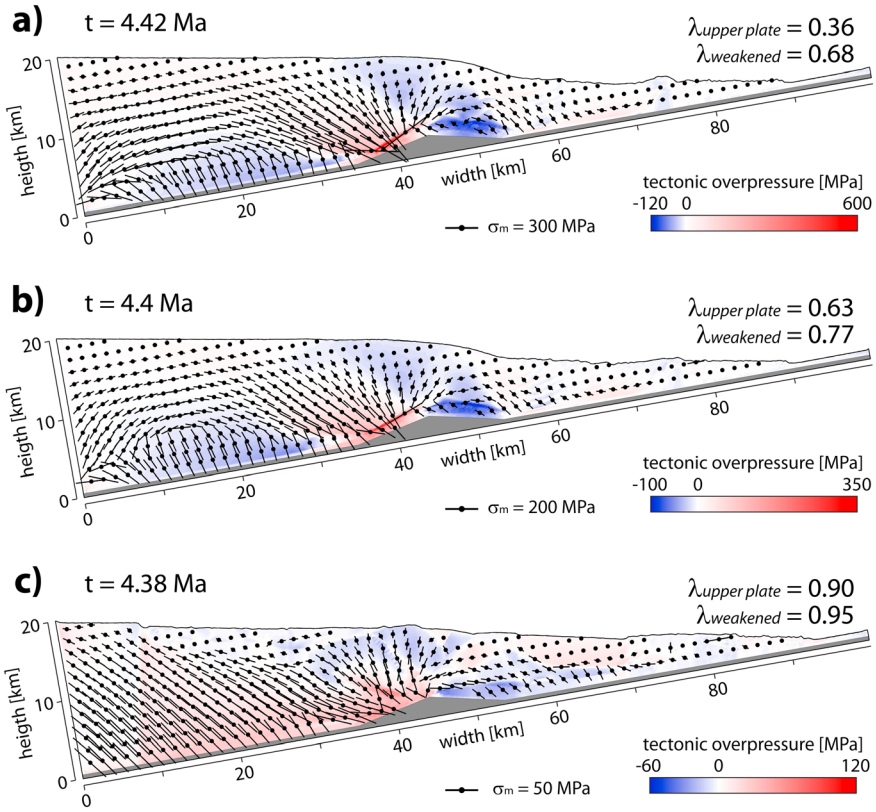

Figure 11. Cross sections at *Ly*/2 of tectonic overpressure and underpressure (deviation from lithostatic pressure) for different upper plate strength with strain weakening and equal subduction interface strength ($\lambda_{interface} = 0.95$) at 4.4 Ma. Rigid lower plate and seamount in grey. (a) $\lambda_{upper\ plate} = 0.36$; $\lambda_{weakened} = 0.68$. (b) $\lambda_{upper\ plate} = 0.63$; $\lambda_{weakened} = 0.77$. (c) $\lambda_{upper\ plate} = 0.9$; $\lambda_{weakened} = 0.95$. Values of tectonic pressure deviation decrease with decreasing upper plate strength. Patterns of dynamic pressure and principal stress orientation are similar for strong and intermediate upper plate strengths (Figures 11a and 11b). Complete gravitational collapse of the margin for very weak upper plate diminishes the influence of the seamount (Figure 11c).

500 m above the interface are similar for experiments with different interface strength. However, as observed in the vertical cross sections of the same experiments (Figure 7), weaker subduction interfaces (increased $\lambda_{interface}$) lead to larger extensional stress fields ahead of the seamount (Figure 8). In the rear part, σ_m are oriented parallel to the seamount outline, rotating to be oriented toward the underpressured area in the wake of the seamounts.

3.3. Effect of Strain Weakening

In addition to the experiments already presented, the effect of strain weakening has been tested on numerical models with different overriding plate strength and intermediate interface strength. Therefore, the overriding plate and seamount strength has been made dependent on accumulated brittle/plastic finite strain. In this study, a linear increase of fluid pressure ratio according to equation (6) and a decrease of cohesion C_0 to 0.2 MPa are applied for $0 < \varepsilon_{pl} < 1$. The accumulated plastic strain after 6 Ma of experiments with and without strain weakening is presented in Figure 9 to illustrate the effect of strain weakening on the structural development of the overriding plate. There, all experiments exhibit increased finite strain values at the frontal prism ($x > 70$ km) due to deformation of incoming material. Apart from the frontal prism, the distribution of accumulated strain differs markedly depending on upper plate strength and whether strain weakening is turned on or not. Experiments without strain weakening and either a strong ($\lambda_{upper\ plate} = 0.36$) or an intermediate upper plate strength ($\lambda_{upper\ plate} = 0.63$) lack localized accumulation of strain within the upper plate (Figures 9a and 9b). However, for $\lambda_{upper\ plate} = 0.9$, conjugated large strain bands rooting down to the interface indicate localized shearing, although the maximum value of $\varepsilon_{pl} = 0.7$ is still relatively low (Figure 9c). Generally, experiments without strain weakening exhibit increased plastic strain in the wake of subducting seamounts in contrast to its surroundings and a gradual decrease to zero ahead of the seamount (Figures 9a–9c).

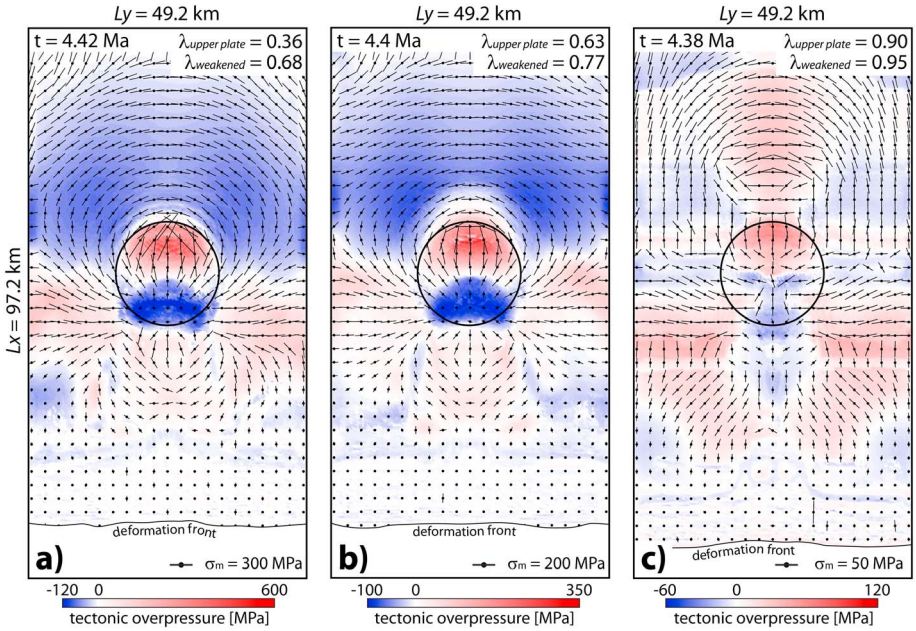

Figure 12. Tectonic overpressure and underpressure (deviation from lithostatic pressure) at the bottom of the overriding plate for different upper plate strength with strain weakening and equal subduction interface strength ($\lambda_{interface} = 0.95$) at 4.4 Ma. (a) $\lambda_{upper\ plate} = 0.36$; $\lambda_{weakened} = 0.68$. (b) $\lambda_{upper\ plate} = 0.63$; $\lambda_{weakened} = 0.77$. (c) $\lambda_{upper\ plate} = 0.9$; $\lambda_{weakened} = 0.95$. Values of tectonic pressure deviation decrease with decreasing upper plate strength. Sizes of large overpressure and underpressure patches are roughly delimited by the seamount extent (black circle) for strong and intermediate upper plate models (Figures 12a and 12b).

Experiments with strain weakening implemented all exhibit specific patterns of localized shear zones (Figures 9d–9f; notice the different scales of color bars). For a fluid pressure ratio of $\lambda_{upper\ plate} = 0.36$ and $\lambda_{weakened} = 0.68$, up to 20 km long narrow thrust shear zones dipping shallowly rearward develop between the seamount and the frontal prism (Figure 9d). This upper plate compression in the wake of the seamount results from gravitational collapse of the bulge. The experiment with intermediate strength ($\lambda_{upper\ plate} = 0.63$; $\lambda_{weakened} = 0.77$) also exhibits subvertical accumulation of strain in the wake of the seamount with a regular spacing of 1.5–2 km (Figure 9e). For $\lambda_{upper\ plate} = 0.9$ ($\lambda_{weakened} = 0.95$), strongly localized strain forms conjugate shear zones rooting into the subduction interface at the trenchward boundary of the seamount (Figure 9f). Furthermore, several sets of conjugate shear zones appear close to the surface in the rear of the margin ($x = 10$–40 km).

Away from the frontal prism, brittle/plastic deformation at the surface of the continental margin is only detectable above the seamount. Only the conjugate shear zones extending to the rear of margin for a weak upper plate ($\lambda_{upper\ plate} = 0.9$) affect the whole width of the model (Figure 10). Vertical cross sections through strong and intermediate margins ($\lambda_{upper\ plate} = 0.36$ and 0.63) with strain weakening show similar patterns of stresses, with peak underpressure and overpressure above the flanks of the seamount and a lower portion of the upper plate under extension (Figures 11a and 11b). For $\lambda_{upper\ plate} = 0.9$, the whole rear part of the margin is overpressured and peaks of overpressure and underpressure are lower compared to the experiment without strain weakening (Figures 5 and 12c).

The upper plate slices 500 m above the interface show that for a strong overriding crust ($\lambda_{upper\ plate} = 0.36$), strain weakening leads to a margin that is underpressured at the rear (Figure 12a), in contrast to the model without strain weakening (Figure 6a). Furthermore, the experiment with large fluid pressure ratio ($\lambda_{upper\ plate} = 0.9$) exhibits a more complex stress pattern, with patches of underpressure and overpressure distributed along the bottom of the overriding plate if strain weakening is implemented (Figure 12c).

3.4. Seamount Deformation

Collision of a seamount with the overriding plate at a subduction zone leads to different patterns of deformation depending on its brittle strength (Figure 9). Accumulated strain shows that the descending seamount only

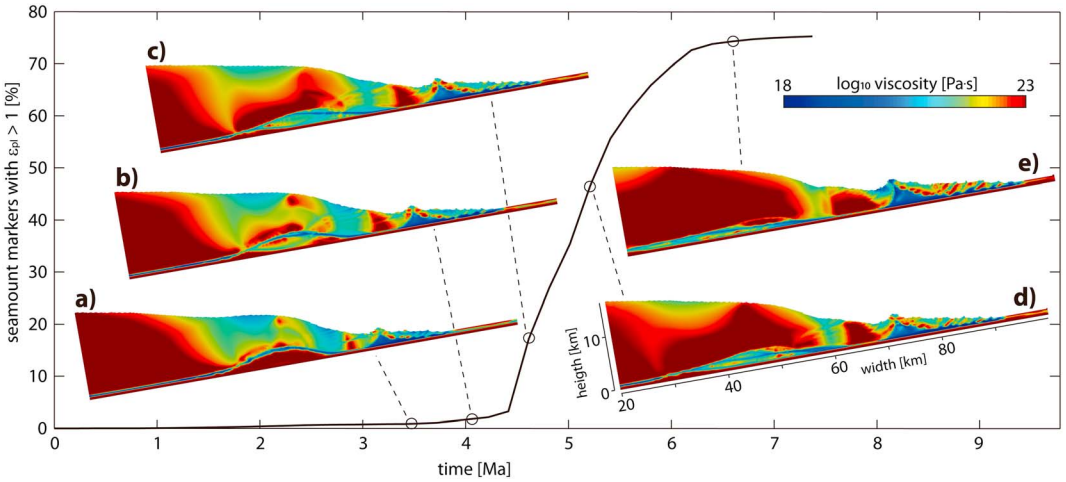

Figure 13. Temporal evolution of seamount deformation of strong upper plate simulation (see Figure 9a). Solid line: Volume percentage of subducting seamount with accumulated plastic strain $\varepsilon_{pl} > 1$. Snapshots of seamount deformation: Cross sections at $Ly/2$ of effective viscosity. (a) Intact seamount. (b) Activation of interface-parallel shear zone deeply rooted in the seamount. (c) Second shear zone deforming the decapitated seamount. (d, e) Further deformation and shearing of the seamount. Scale for all profiles equal to Figure 13d.

gets deformed when the experiment setup has a very strong upper plate ($\lambda_{\text{upper plate}} = 0.36$). In this experiment, at $x = 20$ km, the root of the subducting seamount is still visible, while the largest part was dismembered and strained on its way down, and appears to have been underplated between $x = 30$ and 50 km (Figure 9a). The temporal evolution of seamount deformation for the experiment shown in Figure 9a is illustrated by the percentage of seamount volume exhibiting a finite strain larger than 1 (Figure 13). The seamount remains largely undeformed until 4.3 Ma, after which the volume percentage of strained seamount increases to 70% by 6 Ma. For all other experiments, the volumetric percentage of seamount with a strain larger than 1 remains lower than half a percent until the seamount hits the backstop at $x = 0$.

Cross sections of viscosity at $y = Ly/2$ illustrate the manner in which the seamount deforms during subduction (Figure 13). According to our simplified viscous-brittle/plastic rheological model, effective viscosities lower than $\eta = 10^{23}$ Pa s indicate brittle/plastic failure (Appendix A) and therefore visualize apparent brittle deformation. At 3.4 Ma, the seamount does not exhibit any significant internal deformation (Figure 13a). Shortly after 4 Ma, the initiation of a shear zone crosscutting the seamount at its base is visible (Figure 13b). At 4.6 Ma, almost the complete seamount is failing and brittle strain is accumulated, with a main shear zone that cuts the seamount at its base (Figure 13c). The initially 18 km wide seamount is dismembered along a profile length ~30 km after 5.2 Ma. The initially sheared off seamount is further deformed by a second shear zone cutting off its top (Figure 13d). After 6.6 Ma, the seamount is entirely destroyed and ground down within the subduction interface, thereby also diminishing its effect on deformation within the overriding continental plate (Figure 13e).

4. Discussion and Comparison to Natural Examples

Results demonstrate that the collision of seamounts at active trenches lead to severe brittle deformation of the overriding plate and in certain cases of the seamount. Distribution and magnitude of overpressure and underpressure displayed in vertical cross sections and slices parallel to the subduction interface shows that underthrusting seamounts have a major impact on the stress state within overriding plates. In the following, deformation patterns and topographic evolution of numerical experiments are compared to natural examples of seamount subduction along the Middle America Trench. Here obtained stress fields are discussed with respect to published numerical models and to their potential effect on seismicity along convergent margins.

4.1. Comparison to Topographic Evolution and Upper Plate Deformation of the Middle America Trench

Numerical results are compared to the Middle America Trench offshore Costa Rica and Nicaragua, which have been used as guide for the geometrical setup of our models (section 2). There, the oceanic Cocos Plate

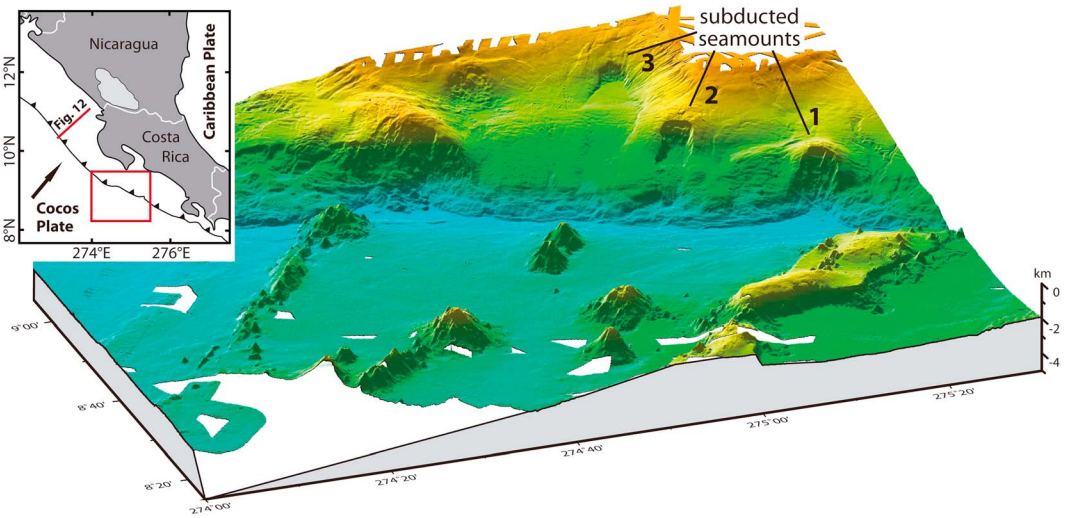

Figure 14. Bathymetry along the Costa Rica active margin. See inlet for location (red square). Seamounts on the incoming plate (center) have diameters of approximately 20 km and are 2–2.5 km high. In the southern part, three areas of seamount collision into continental slope can be observed from bathymetry. Seamount 1: Early stage with unclosed reentrant and large bulge atop seamount. Seamount 2: Reentrant closed, frontal prism recovered, and less explicit bulge. Seamount 3: Undeformed filling of seamount scar and absence of a bulge indicate further subduction or dismembering of the seamount.

subducts northeastward below the continental Caribbean Plate at a rate of ~9 cm/yr [*DeMets et al.*, 1990]. The Middle America Trench is considered to experience tectonic erosion, where removed mass from the bottom of the upper plate leads to extension and subsidence of the continental margin [*Ranero and von Huene*, 2000; *Vannucchi et al.*, 2003]. Additionally, colliding seamounts influence the structural evolution of the overriding plate. Offshore Costa Rica, seamounts with heights between 2 and 2.5 km and diameters of ~20 km and are scattered on the oceanic plate [*von Huene et al.*, 2000]. Along the continental slope, a series of seafloor embayments have been mapped and interpreted to result from seamount subduction (Figure 14). Between 275°E and 275°20′E, three furrows traverse the margin marking three different stages of seamount subduction (marked 1–3 in Figure 14). Gravitational collapse occurs in the wake of all these seamounts. The scar caused by seamount 1 is defined by a reentrant of the trench axis where the frontal sedimentary prism has not yet recovered. For the deeper-into-the-subduction seamounts 1 and 2, the frontal prism has been reestablished. Topographic bulges are observed atop seamounts 1 and 2, with the one above seamount 1 being more significant (Figure 14). The lack of a topographic bulge over seamount 3 could indicate that this seamount has subducted further below the shelf or has been destroyed. This is supported by the inactivity of the collapsing wake, indicated by undisturbed sedimentary filling of the furrow (Figure 14). However, clustering of seamounts under the shelf has been interpreted to support the presence of largely intact seamounts [*von Huene et al.*, 2000], one of those having been imaged with seismic tomography [*Husen et al.*, 2002]. The trench reentrant and bulge at 274°40′ indicates a larger underthrust seamount, destabilizing a large part of the continental slope.

Observed natural topographic features from offshore Costa Rica are compatible with most modeling results presented here, except for the simulation with a strong upper plate ($\lambda_{\text{upper plate}} = 0.36$) and no weakening, where the seamount is destroyed during descendence (Figures 9a, 10a, and 13), and for the simulation with $\lambda_{\text{upper plate}} = 0.9$ and $\lambda_{\text{weakened}} = 0.95$, where the complete margin collapses gravitationally independent of the entering seamount (Figures 9f and 10f). The topographic evolution of all other experiments is similar and best illustrated by the reference model (Figure 4). There, the seafloor bulge diminishes from ~2 km to ~500 m as the seamount subducts deep under the margin (Figures 4a–4d). This is similarly observed along the Costa Rica trench and indicates that a larger bulge (seamount 1) close to the trench axis does not imply a larger seamount (Figure 14). The colliding seamount initially provokes a reentrant in the frontal prism (Figures 3a and 4e) that is closed soon after the seamount fully underthrusts the continental slope (Figures 3b and 4f), comparable to seamounts 1 and 2 (Figure 14). Lateral ridges in the wake of numerical seamounts define a width of a furrow roughly equal to the seamount width at depth (Figure 4). This suggests similarly large seamounts 1–3 under the Costa Rica margin (Figure 14).

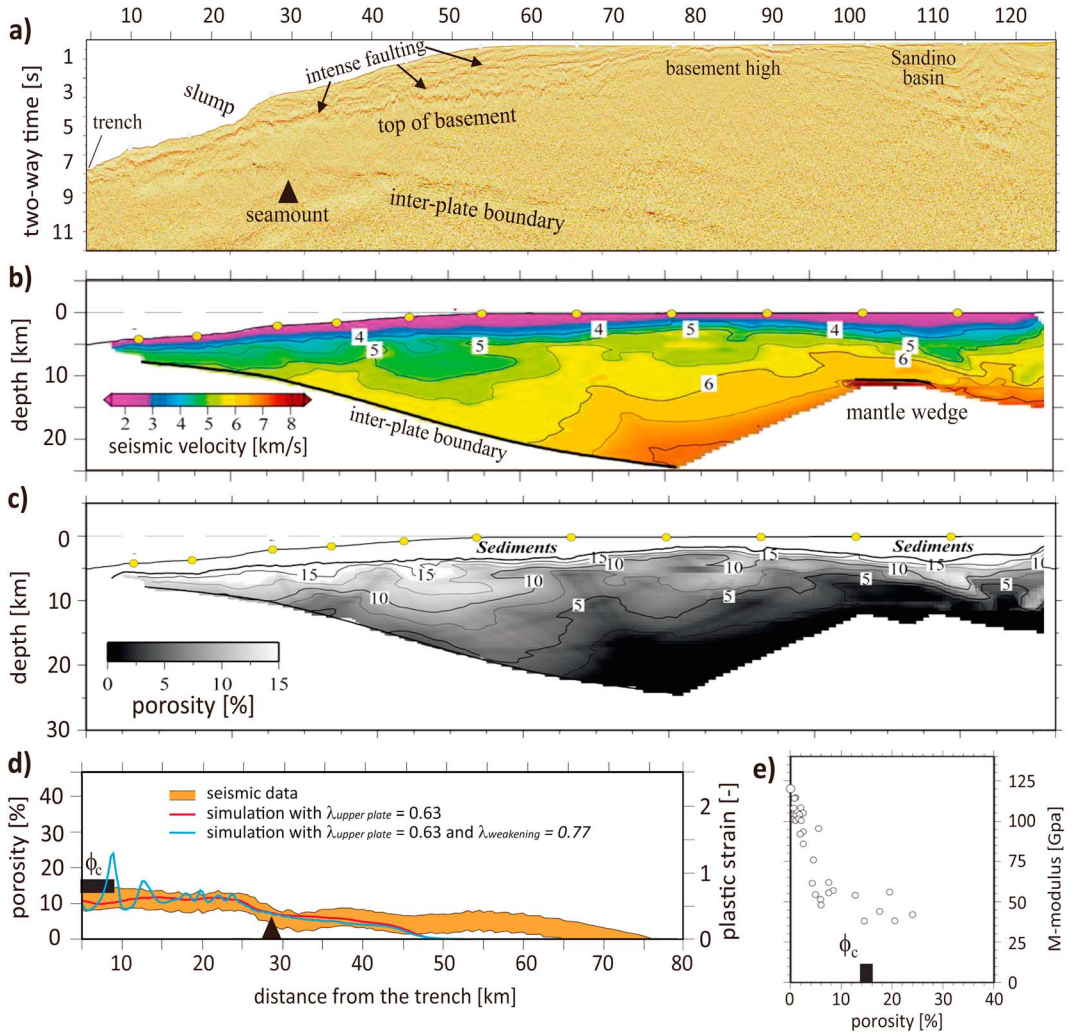

Figure 15. (a) Poststack time-migrated multichannel seismic (MCS) reflection dip line NIC-20, acquired perpendicular to the continental margin from the outer rise to near the coast line (see inlet in Figure 14 for location). The image shows the continuity of the plate boundary reflective zone. The top of basement is marked by a clear reflection under the slope that reaches trench, showing a pronounced thinning toward the trench axis with essentially no accretionary wedge. The Sandino Basin is compartmentalized in two subbasins by an uplifted basement high. The region is cut by abundant normal faults. Black triangle shows the subducted seamount location. (b) 130 km long section of a *P* wave velocity model of the overriding plate and geometry of the interplate boundary reflector obtained using ocean bottom hydrophones (OBH, yellow circles) deployed along the same line. The model has been obtained by joint reflection and refraction traveltime inversion [*Sallares et al*., 2013]. Interplate and upper plate Moho reflectors are represented by thick black lines. Isovelocity contours in the sediments are not shown for clarity. (c) Porosity model calculated using the *P* wave velocity model shown in Figure 15b. To convert velocity into porosity, we assume that the overriding plate basement is made of igneous rocks (basalts), so we have applied an empirical relationship based on data compilation for this rock type, shown in Figure 15e. Black tick indicates the critical porosity (ϕ_c) for water-saturated basalts [*Nur et al*., 1998]. Sediments are excluded from the calculation. (d) Average porosity along a 1 km thick band just above the interplate boundary, as a function of the distance from the trench, using the *P* wave velocity model shown in Figure 15b. The width of the orange band reflects V_p uncertainty. Black triangle shows the subducted seamount location. Solid lines: accumulated plastic/brittle strain 2 km above the interface indicating fracturing of overriding plate with intermediate upper plate strength. Red line: no strain weakening. Blue line: strain weakening. (e) M-Modulus/porosity diagram for water-saturated basalts. Black tick indicates critical porosity (ϕ_c) estimated from this particular data set. Data are from *Nur et al*. [1998].

A seismic reflection profile imaging the continental margin offshore Nicaragua (inlet in Figure 14 for location) illustrates a subducted seamount below the slope approximately 30 km landward from the trench axis (Figure 15a). Similar to the continental margin offshore Costa Rica, there are the topographic bulge atop the seamount and a large-scale gravitational collapse of the slope, i.e., landsliding above the trenchward flank of the seamount

(Figure 15a). Intense trenchward dipping normal faulting along the upper slope area indicates that the margin is generally in extensional tectonic mode. This is consistent with the concept of subduction erosion, which is interpreted to take place along the Middle America margin [*Vannucchi et al*., 2003; *von Huene et al*., 2004]. Material is removed from the bottom of the overriding plate leading to constant subsidence of the slope. Normal faults indicate that the slope taper should be roughly in the order of the maximal critical taper angle [*Davis et al*., 1983]. This furthermore explains why bulges formed due to subducting seamounts that collapse gravitationally. Numerical results presented here support general extensional tectonics for the Middle America margin. Even though basal erosion is ignored in the experiments (thickness of eroding horizon is in the order of implemented numerical interface thickness of 400 m [*von Huene et al*., 2004]), continental margins are overall in extension (Figures 5–8). Large deep-rooted normal faults only develop within very weak upper plates ($\lambda_{\text{upper plate}} = 0.9$). Those experiments are therefore in a supercritical state according to the analytical critical wedge theory, whereas the experiments with a stronger upper plate plot in the stable area [*Davis et al*., 1983].

Joint reflection and refraction traveltime inversion of wide-angle seismic data collocated with the seismic reflection profile (Figure 15) provided a *P* wave velocity (V_p) model of the upper plate and geometry of the boundary reflector of the plate interface. The degree of rock fracturing/porosity (Figure 15c) was calculated from V_p using existing empirical relationships for fractured basalts as in *Sallares and Ranero* [2005] (Figure 15e). The method used to calculate V_p and to transform it to fracturing/porosity values is explained in Appendix B. Average porosity values along a 1 km thick horizon above the interplate boundary indicate intense upper plate fracturing that concentrates in the wake of the subducted seamount and abruptly decreases landward of the location of the subducted seamount (Figure 15d). Porosity values are everywhere below the critical limit, which means that the rock is still able to transmit stresses and store elastic energy. This could explain why this part of the interplate boundary fault ruptured coseismically during an event in 1992 even if the upper plate was severely damaged by the seamount [*Sallares et al*., 2013]. A similar spatial distribution of fracturing is also estimated from the numerical results. Accumulated plastic strain (quasi-brittle fracturing) above the subduction interface shows a similar trend as V_p-derived porosity values (Figure 15d). Combined seismic and numerical results indicate severe brittle deformation of the overriding plate due to seamount indentation, where the fractured corridor has the width of the tunneling seamount (Figure 10).

4.2. Impact of Subducting Seamounts on Stress States Along Continental Margins

Numerical results concerning stress states have to be taken into account with care due to the fact that elasticity is ignored in the numerical formulation. Nevertheless, the models provide realistic first-order long-term stress state estimates, which are mostly defined by the brittle strength (i.e., fluid pressure ratio) of the upper plate. The applied modeling strategy included testing the influence of upper plate strength, interface strength, and rheological weakening due to finite accumulated deformation. Results show that a general pattern of overpressure and underpressure as well as principal stress directions can be inferred independent of upper plate or interface strength: all cross sections (except simulation with $\lambda_{\text{weakened}} = 0.95$; Figure 10c) illustrate major areas of overpressure above the leading flank of the seamount and underpressure above the trenchward flank (Figures 5, 7, and 11). Overpressured areas extend rearward and upward in all simulations. Furthermore, experiments display an underpressured triangle zone above the seamount reaching the seafloor as well as above the plate interface ahead the seamount (Figures 5, 7, and 11). The similarity of obtained stress patterns leads to the conclusion that these are characteristic for convergent margins during seamount underthrusting. The magnitude of overpressure and underpressure areas depends on upper plate strength, i.e., the plastic stress envelope (Figure 5). Investigated interface strength has a minor effect on stress evolution in the overriding plate (Figure 7), although only a very narrow range of interface strength values was applied here. Indeed, *Baba et al*. [2001] proposed a similar pattern of minimum and maximum incremental shear stresses around an indenting seamount. Three-dimensional numerical models of aseismic ridge subduction indicate a similar evolution of vertical displacement rates and development of reentrants along the subduction trench [*Zeumann and Hampel*, 2015]. Like in experiments presented here, their obtained stress field patterns are delineated by the extent of the underthrust ridge. Differences in absolute values are due to upper plate strength and the geometrical inequality of ridges and seamounts.

Overpressure and underpressure are equivalent to compressional and extensional stress states, respectively (Figure 2b). The major overpressure area atop the leading flank of the subducting seamount shows principal stress directions suborthogonal to the seamount flank and results from the pushing up of the

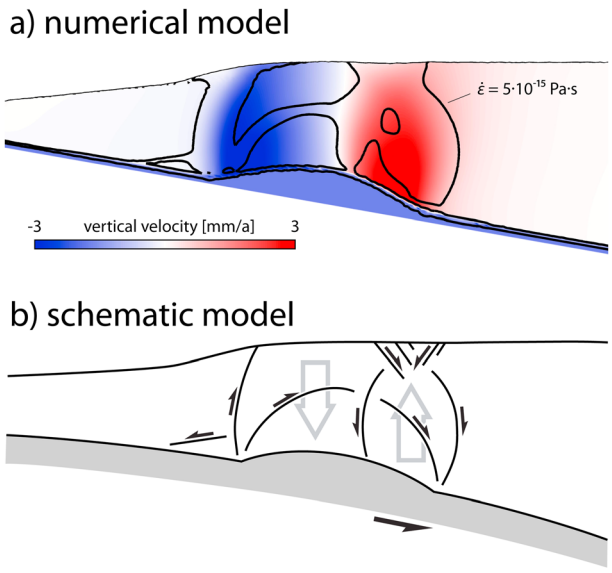

Figure 16. Instantaneous deformation of the continental margin during seamount subduction illustrated by reference model. (a) Vertical velocities at the surface of the overriding plate. Contours indicate strain rate of $\dot{\varepsilon} = 5 \cdot 10^{-15}\,s^{-1}$. (b) Schematic model inferred from numerical results shown in Figure 16a. Subvertical fault zones (black arrows) divide uplifting and descending parts of the upper plate atop the rearward and the trenchward flanks of the seamount, respectively (grey arrows).

overriding plate by the underthrusting seamount (Figures 5, 7, and 11). This upward push of the margin leads to extensional differential stresses along the rearward bottom of the upper plate due to bending. These differential stresses are below the yield stress (Figure 3) and would be less prominent if elastic deformation would be additionally implemented. The extensional triangle zone atop the seamount forms the topographic bulge (Figures 4 and 14) and results from plate bending. Due to low confining pressure close to the surface, stresses are defined by the yield strength and extensional fractures and small offset normal faults cut the topographic bulge (Figure 3) as it is commonly observed in seafloor maps (Figure 14). A pressure shadow zone characterized by underpressure develops in the wake of the seamount (Figures 5, 7, and 11). Slices near the bottom of overriding continental plates illustrate that the areas of large overpressure and underpressure are delimited by the extent of the subducting seamount (Figures 6, 8, and 12), resulting in a heterogeneous stress field that has potential to influence the stress regime along the actual subduction interface. An exception is the experiment with $\lambda_{\text{upper plate}} = 0.9$ and $\lambda_{\text{weakened}} = 0.95$ (Figures 9f, 10c, 11c, and 12c), where the complete shelf collapses gravitationally, independent of seamount indentation.

4.3. Potential Implications for Seismogenesis

There has been a long-lasting, still ongoing discussion about the influence of rough seafloor topography [e.g., *Das and Watts*, 2009; *Wang and Bilek*, 2014] and of single seamounts [e.g., *Wang and Bilek*, 2011; *Watts et al.*, 2010] on subduction zone seismicity. Some studies report that seamounts act as barriers for earthquake rupture propagation [*Kodaira et al.*, 2000; *Singh et al.*, 2011]. In other cases, earthquakes have been spatially related to the occurrence of subducted seamounts and interpreted to be related to rupture asperities [*Bell et al.*, 2014; *Sallares et al.*, 2013]. It appears that epicenters are located at the leading flank of underthrusting seamounts and that main slip occurs deeper, away from but near the seamount [*Abercrombie et al.*, 2001; *Geersen et al.*, 2015; *Mochizuki et al.*, 2008]. Furthermore, *Mochizuki et al.* [2008] argued that the width of the rupture area can be influenced by that of the seamount, which can also be true for two earthquakes related to seamounts in Costa Rica [*Bilek et al.*, 2003, Figure 1]. *Abercrombie et al.* [2001] showed that all aftershock mechanisms of the seamount-related 1994 Java earthquake exhibited normal faulting, most of them along the trenchward flank of the subducted seamount. The fact that seamounts can act either as barriers or as sources for earthquake rupture does not need to be contradictory. The 2014 Iquique earthquake partly ruptured the Northern-Chile seismic gap [*Schurr et al.*, 2014]. Toward the south, rupture propagation ceased perhaps due to an area of lower plate coupling. This low coupled area spatially correlates with two subducted seamounts [*Geersen et al.*, 2015]. Two days later, a 7.6 M_w aftershock occurred at the landward extension of the seamount, propagating mainly landward [*Geersen et al.*, 2015]. In both cases, seamounts appear to have hindered the rupture to propagate.

The plate coupling pattern in North Chile illustrates that there, seamounts are not pinning the fault locally, as mentioned as a general possibility by *Zhan et al.* [2012]. *Wang and Bilek* [2011] explained this by pervasive brittle weakening of the upper plate related to seamount indentation. An overriding plate fault pattern has

been established from observed surface deformation of analogue models [*Dominguez et al*., 1998b]. This stands in contrast to earlier interpretations by *Scholz and Small* [1997], who suggested that the purely elastic bending of the upper plate during seamount subduction increases the normal stress locally. Numerical experiments and seismic interpretations presented here report intense brittle deformation of the continental margin above subducting seamounts (Figures 9 and 15). An instantaneous fracturing pattern inferred from numerical strain rates shows subvertical fault zones at the trenchward and rearward extremities of the seamount and one above its center, dividing zones of push-up and gravitational relaxation (Figure 16). The pushed-up area above the leading flank of subducting seamounts defines the location of the topographic bulge, which undergoes extension (normal faulting) due to upward bending.

Patterns of deformation, overpressure and underpressure, and principal stresses presented in this study can qualitatively explain natural observations related to earthquake propagation, occurrence, and upper plate brittle fracturing, which appear to be strongly linked. The numerical stress field at the bottom of the overriding plate is strongly heterogeneous with increased stresses at the leading flank of the seamount. These numerical results are consistent with the abrupt increase of upper plate fracturing that occurs in the wake of a subducted seamount in the Nicaragua margin (Figure 15d). The extreme change in stress state toward the seamount potentially influences the subduction interface, ceasing arriving fault ruptures. On the other hand, the overpressured area itself can be a potential source of earthquakes rupturing a relatively small area (Figures 6, 7, and 12). This matches the argumentation that rupture areas related to earthquakes located at seamount extremities are in order of the width of the seamounts themselves [*Bilek et al*., 2003; *Mochizuki et al*., 2008]. Large overpressure values over those areas could indicate that such seismic events potentially experience large stress drops. Furthermore, such earthquakes are potentially dangerous as they can occur close to the subduction trench and generate tsunamis. This model has been proposed for the 1947 Hikurangi [*Bell et al*., 2014] and the 1992 Nicaragua [*McIntosh et al*., 2007; *Sallares et al*., 2013] tsunami earthquakes. Furthermore, reported extensional aftershocks above the trenchward seamount flank of the 1994 Java earthquake [*Abercrombie et al*., 2001] match the predicted underpressure (extensional) zone in numerical experiments (Figures 5–8, 11, and 12).

5. Conclusion

A high-resolution three-dimensional finite difference model was used to investigate brittle/plastic deformation and stress distribution within active continental margins during seamount subduction. Different upper plate and subduction interface strength was applied depending on the fluid pressure ration λ. Additionally, simulations with a strain weakening effect were tested. Numerical results show that indenting seamounts strongly deform the overriding plate on a corridor as wide as the underthrusting seamount by constantly shifting subvertical shear zones rooted at the seamount extensions. A reentrant develops during initial seamount collision, as well as a topographic bulge atop the seamount and lateral ridges when the seamount subducts further. Strain weakening leads to a slightly more localized fracture system, but displacement remains generally little.

Patterns of overpressure and underpressure reveal that margins are generally under extension, due to their super-critical taper. Indenting seamounts result in strongly overpressured areas of the upper plate above the rearward and underpressured above the trenchward seamount flank, respectively. Overpressured and underpressured zones are spatially roughly identical with seamount extension. Absolute values depend on upper plate strength.

Numerical experiments reproduce observations from the Middle America Trench, such as reentrants along the frontal prism, bulges atop, and furrows delineated by ridges in the wake of subducting seamounts offshore Costa Rica. Porosity values derived from a *P* wave velocity model along a profile offshore Nicaragua indicate intense fracturing of the upper plate by seamount indentation. Numerical results support strong brittle overriding plate deformation. *Wang and Bilek* [2011] proposed that intense fracturing of the upper plate prevents great earthquake occurrence where large seamounts subduct.

A long-standing question in subduction dynamics is whether seamounts act as barriers or asperities for large and giant earthquakes. Numerical experiments presented here support observations from different earthquake rupture histories: (i) The very heterogeneous stress field around subducting seamounts and the deformation of the overriding plate acts as a barrier for the propagation of earthquake rupture surfaces sourced at a smooth part of the subduction interface and (ii) large overpressure areas with a width similar to that of the subducting seamount can trigger large stress drop, relatively small rupture surface

earthquakes, with large slip values downward from the seamount, and extensional aftershocks above the trenchward flank.

Appendix A: Numerical Methods

A1. Governing Equations

The applied numerical code has been used in earlier studies to investigate critical taper mechanics in accretionary wedges [*Ruh et al*., 2013, 2014] and is based on a three-dimensional, high-resolution, fully staggered grid, finite difference, marker-in-cell model with a visco-brittle/plastic rheology. Equations of mass conservation (assuming incompressibility)

$$\frac{\partial u_i}{\partial x_i} = 0, \tag{A1}$$

and the conservation of momentum (Stokes equation)

$$\frac{-\partial P}{\partial x_i} + \frac{\partial \tau_{ij}}{\partial x_j} = \rho g_i \tag{A2}$$

are solved with an efficient OpenMP-parallelized multigrid solver (I3ELVIS) [*Gerya*, 2010; *Gerya and Yuen*, 2007]. u_i = velocity ($u_1 = u_x$, $u_2 = u_y$, $u_3 = u_z$), x_i = spatial coordinates ($x_1 = x$, $x_2 = y$, $x_3 = z$), P = dynamic pressure, ρ = density, g_i = gravitational acceleration ($g_1 = g_2 = 0$, $g_3 = 9.81$ m/s^2), and τ_{ij} = deviatoric stress tensor:

$$\tau_{ij} = 2\eta\dot{\varepsilon}_{ij}, \tag{A3}$$

where η = viscosity and $\dot{\varepsilon}_{ij}$ = strain-rate tensor:

$$\dot{\varepsilon}_{ij} = \frac{1}{2}\left(\frac{\partial u_i}{\partial x_j} + \frac{\partial u_j}{\partial x_i}\right). \tag{A4}$$

Differential stresses exceeding yield stresses lead to plastic failure according to the Drucker-Prager yield criterion:

$$F = \tau^{II} - \sigma_y \tag{A5}$$

where τ^{II} = second invariant of the stress tensor:

$$\tau^{II} = \sqrt{\frac{1}{2}\tau_{ij}^2} \tag{A6}$$

and σ_y = yield stress:

$$\sigma_y = P{\cdot}\sin\phi + C{\cdot}\cos\phi \tag{A7}$$

with C = cohesion and ϕ = internal friction angle.

A2. Numerical Implementation

The system of equations based on the discretization of equation (A3) is solved implicitly with an efficient OpenMP-parallelized multigrid solver on 16 threads. Visco-brittle/plastic strain rates are obtained by a standard effective viscosity implementation [e.g., *Buiter et al*., 2006, and reference therein]. For stresses below the yield stress, the model rheology is linear viscous. When stresses reach the yield stress, effective viscosities η are depressed, according to

$$\eta_{vp} = \frac{\sigma_y}{2\dot{\varepsilon}^{II}}, \tag{A8}$$

where σ_y = yield stress, η_{vp} = plastic effective viscosity, and $\dot{\varepsilon}^{II}$ = second invariant of the strain-rate tensor:

$$\dot{\varepsilon}^{II} = \sqrt{\frac{1}{2}\dot{\varepsilon}_{ij}^2}. \tag{A9}$$

Time steps are taken small to ensure very small changes of stress and strain-rate state of the markers so that no further iterations are needed. Benchmarking of this approach shows that the solution does not significantly change by adding more iterations [*Gerya*, 2010, chap. 13, exercise 13.2].

Appendix B: Seismic Profile Offshore Nicaragua

The *P* wave velocity model in Figure 15 has been modeled by joint reflection and refraction traveltime inversion of seismic refractions within the upper plate sediments and basement (Pg) and reflections at the interplate boundary (PiP), using *tomo2d* [*Korenaga et al*., 2000]. For this we used refraction and wide-angle reflection seismic (WAS) data recorded at 11 ocean bottom hydrophones (OBH) along the 160 km long NIC-20 profile, which runs from the outer rise to the coast line (see Figure 14 for location). This WAS profile was acquired in 2000 as part of the EW00-05 cruise performed by the U.S. R/V *Maurice Ewing*. Details on the acquired data set, inversion method, model parameterization, and regularization parameters are given in *Sallares et al*. [2013]. The *P* wave velocity was converted to porosity assuming that the upper plate basement of this erosional margin is made of igneous rocks, and there is no accretionary prism [e.g., *McIntosh et al*., 2007; *Sallares et al*., 2013]. Therefore, the strong lateral velocity gradient (Figure 15b) is assumed to be caused by variations in the rock fracturing degree, fluid content, and alteration, rather than lithological changes. We have estimated the rock fracturing/porosity degree (ϕ) based on *P* wave velocity (V_p) applying available empirical relationships for fractured, fluid-saturated basalts as in *Sallares and Ranero* [2005] (Figure 15e). The parameter used to calculate ϕ as a function of V_p is the critical porosity (ϕ_c), which is a threshold value above which the rock is considered to be disaggregated, so no loads or stresses can be accumulated or transmitted: the unaltered rock velocity, V_R, and the velocity at the critical porosity, V_c. Based on experimental results, combined with the results from our model, we obtain $V_R \approx 6.5$ km/s and $V_c \approx 4.3$ km/s, so $\phi_c \approx 0.15$ [*Nur et al*., 1998; *Sallares and Ranero*, 2005]. This indicated that if we assume that the upper plate basement is constituted be oceanic basalt [e.g., *McIntosh et al*., 2007], the margin segments displaying velocities below ~4.3 km/s ($\phi > 0.15$) are likely to be disaggregated and mostly fluid supported. In contrast, when velocity is above ~4.3 km/s ($\phi < 0.15$), one can estimate rock porosity using the above values, which gives $\phi = 0.46–0.07V_p$. More details on the calculations are given in *Sallares and Ranero* [2005]. Finally, we have calculated rock porosity within a 1 km thick band at the interplate boundary to estimate the variations of rock properties in the area that is likely to be most affected by the subduction of the incoming plate. The obtained results are shown in Figure 15d. In this figure, the V_p uncertainty corresponds to the average of the values obtained by statistical uncertainty analysis following a statistical method explained in *Sallares et al*. [2013]. The porosity shows an overall decrease between the trenches, where it is close to ϕ_c, to 70–80 km from the trench, where it is insignificant. It is interesting to note, however, that the increase in porosity is not linear. Most of it occurs in <5 km, just on top of the subducted seamount. The correspondence between the position of the subducted seamount and the sharp porosity increase of the bottom of the overriding plate strongly indicates that the seamount is probably responsible for most of the upper plate fracturing.

The multichannel seismic (MCS) line shown in Figure 15 was acquired coincident with the WAS during the EW00-05 experiment, using a 6 km long streamer of 240 channels (25 m of channel spacing) and a sampling rate of 2 ms. The airgun array had a volume of 6835 cubic inches, whereas the shot distance was 50 m. The MCS processing flow included noisy traces of elimination, amplitude compensation of geometrical spreading, statistical predictive deconvolution, trace muting and stacking, time- and space-variant band-pass filtering, and finally, poststack time migration. For additional details in the processing sequence see *McIntosh et al*. [2007].

Acknowledgments

Funding was received from the People Programme (Marie Curie Actions) of the European Union's Seventh Framework Programme FP7/2007-2013/ under REA grant agreement 604713 (ZIP "Zooming In between Plates"). V.S. and C.R.R. acknowledge financial support received through the HADES project (CTM2011-30400-C01 and CTM2011-30400-C02), funded by Spanish MINECO. The authors thank Roland von Huene and an anonymous reviewer for their constructive comments. Thanks also go to Dennis Brown and Neil Mancktelow for their valuable comments concerning the linguistic representation. Numerical data have been processed using Paraview and MATLAB and are available upon request from the corresponding author. Anyone interested in seismic and bathymetric data will be directed to according databases.

References

Abercrombie, R. E., M. Antolik, K. Felzer, and G. Ekstrom (2001), The 1994 Java tsunami earthquake: Slip over a subducting seamount, *J. Geophys. Res.*, *106*(B4), 6595–6607, doi:10.1029/2000JB900403.

Baba, T., T. Hori, S. Hirano, P. R. Cummins, J. O. Park, M. Kameyama, and Y. Kaneda (2001), Deformation of a seamount subducting beneath an accretionary prism: Constraints from numerical simulation, *Geophys. Res. Lett.*, *28*(9), 1827–1830, doi:10.1029/2000GL012266.

Bangs, N. L., S. P. S. Gulick, and T. H. Shipley (2006), Seamount subduction erosion in the Nankai Trough and its potential impact on the seismogenic zone, *Geology*, *34*(8), 701–704.

Bangs, N. L., K. D. McIntosh, E. A. Silver, J. W. Kluesner, and C. R. Ranero (2015), Fluid accumulation along the Costa Rica subduction thrust and development of the seismogenic zone, *J. Geophys. Res. Solid Earth*, *120*, 67–86, doi:10.1002/2014JB011265.

Bell, R., C. Holden, W. Power, X. M. Wang, and G. Downes (2014), Hikurangi margin tsunami earthquake generated by slow seismic rupture over a subducted seamount, *Earth Planet. Sci. Lett.*, *397*, 1–9.

Bilek, S. L., S. Y. Schwartz, and H. R. DeShon (2003), Control of seafloor roughness on earthquake rupture behavior, *Geology*, *31*(5), 455–458.

Buiter, S. J. H., A. Y. Babeyko, S. Ellis, T. V. Gerya, B. J. P. Kaus, A. Kellner, G. Schreurs, and Y. Yamada (2006), The numerical sandbox: Comparison of model results for a shortening and an extension experiment, in *Analogue and Numerical Modelling of Crustal-Scale Processes*, *Geol. Soc. Spec. Publ.*, vol. 253, edited by S. J. H. Buiter and G. Schreurs, pp. 29–64.

Byerlee, J. (1978), Friction of rocks, *Pure Appl. Geophys.*, *116*(4-5), 615–626.

Cloos, M. (1992), Thrust-type subduction-zone earthquakes and seamount asperities: A physical model for seismic rupture, *Geology*, *20*(7), 601–604.
Cloos, M., and R. L. Shreve (1996), Shear-zone thickness and the seismicity of Chilean- and Marianas-type subduction zones, *Geology*, *24*(2), 107–110.
Collot, J. Y., and M. A. Fisher (1989), Formation of fore-arc basins by collision between seamounts and accretionary wedges: An example from the New Hebrides subduction zone, *Geology*, *17*(10), 930–933.
Cubas, N., J. P. Avouac, P. Souloumiac, and Y. Leroy (2013), Megathrust friction determined from mechanical analysis of the forearc in the Maule earthquake area, *Earth Planet. Sci. Lett.*, *381*, 92–103.
Das, S., and A. B. Watts (2009), Effect of subducting seafloor topography on the rupture characteristics of great subduction zone earthquakes, in *Subduction Zone Geodynamics*, *Front Earth Sci. Ser.*, edited by S. Lallemand and F. Funiciello, pp. 103–118, Springer, Berlin.
Davis, D., J. Suppe, and F. A. Dahlen (1983), Mechanics of fold-and-thrust belts and accretionary wedges, *J. Geophys. Res.*, *88*(Nb2), 1153–1172, doi:10.1029/JB088iB02p01153.
DeMets, C., R. G. Gordon, D. F. Argus, and S. Stein (1990), Current plate motions, *Geophys. J. Int.*, *101*(2), 425–478.
Dominguez, S., S. Lallemand, J. Malavieille, and P. Schnurle (1998a), Oblique subduction of the Gagua Ridge beneath the Ryukyu accretionary wedge system: Insights from marine observations and sandbox experiments, *Mar. Geophys. Res.*, *20*(5), 383–402.
Dominguez, S., S. Lallemand, J. Malavieille, and R. von Huene (1998b), Upper plate deformation associated with seamount subduction, *Tectonophysics*, *293*(3-4), 207–224.
Dominguez, S., J. Malavieille, and S. Lallemand (2000), Deformation of accretionary wedges in response to seamount subduction: Insights from sandbox experiments, *Tectonics*, *19*(1), 182–196, doi:10.1029/1999TC900055.
Duan, B. C. (2012), Dynamic rupture of the 2011 M_w 9.0 Tohoku-Oki earthquake: Roles of a possible subducting seamount, *J. Geophys. Res.*, *117*, B05311, doi:10.1029/2011JB009124.
Dymkova, D., and T. Gerya (2013), Porous fluid flow enables oceanic subduction initiation on Earth, *Geophys. Res. Lett.*, *40*, 5671–5676, doi:10.1002/2013GL057798.
Geersen, J., C. R. Ranero, U. Barckhausen, and C. Reichert (2015), Subducting seamounts control interplate coupling and seismic rupture in the 2014 Iquique earthquake area, *Nat. Commun.*, *6*, 8267, doi:10.1038/ncomms9267.
Gerya, T. (2010), *Introduction to Numerical Geodynamic Modelling*, pp. 345, Cambridge Univ. Press, Cambridge, U. K.
Gerya, T., and D. A. Yuen (2007), Robust characteristics method for modelling multiphase visco-elasto-plastic thermo-mechanical problems, *Phys. Earth Planet. Inter.*, *163*(1-4), 83–105.
Hampel, A., J. Adam, and N. Kukowski (2004), Response of the tectonically erosive south Peruvian forearc to subduction of the Nazca Ridge: Analysis of three-dimensional analogue experiments, *Tectonics*, *23*, TC5003, doi:10.1029/2003TC001585.
Hensen, C., and K. Wallmann (2005), Methane formation at Costa Rica continental margin—Constraints for gas hydrate inventories and cross-decollement fluid flow, *Earth Planet. Sci. Lett.*, *236*(1-2), 41–60.
Hillier, J. K., and A. B. Watts (2007), Global distribution of seamounts from ship-track bathymetry data, *Geophys. Res. Lett.*, *34*, L13304, doi:10.1029/2007GL029874.
Husen, S., E. Kissling, and R. Quintero (2002), Tomographic evidence for a subducted seamount beneath the Gulf of Nicoya, Costa Rica: The cause of the 1990 M_w = 7.0 Gulf of Nicoya earthquake, *Geophys. Res. Lett.*, *29*(8), 1238, doi:10.1029/2001GL014045.
Isozaki, Y., S. Maruyama, and F. Furuoka (1990), Accreted oceanic materials in Japan, *Tectonophysics*, *181*(1-4), 179–205.
Kodaira, S., N. Takahashi, A. Nakanishi, S. Miura, and Y. Kaneda (2000), Subducted seamount imaged in the rupture zone of the 1946 Nankaido earthquake, *Science*, *289*(5476), 104–106.
Korenaga, J., W. S. Holbrook, G. M. Kent, P. B. Kelemen, R. S. Detrick, H. C. Larsen, J. R. Hopper, and T. Dahl-Jensen (2000), Crustal structure of the southeast Greenland margin from joint refraction and reflection seismic tomography, *J. Geophys. Res.*, *105*(B9), 21,591–21,614, doi:10.1029/2000JB900188.
Lallemand, S., and X. Le Pichon (1987), Coulomb wedge model applied to the subduction of seamounts in the Japan Trench, *Geology*, *15*(11), 1065–1069.
Lallemand, S., J. Malavieille, and S. Calassou (1992), Effects of oceanic ridge subduction on accretionary wedges: Experimental modeling and marine observations, *Tectonics*, *11*(6), 1301–1313, doi:10.1029/92TC00637.
Lallemand, S., P. Schnurle, and J. Malavieille (1994), Coulomb theory applied to accretionary and nonaccretionary wedges: Possible causes for tectonic erosion and or frontal accretion, *J. Geophys. Res.*, *99*(B6), 12,033–12,055, doi:10.1029/94JB00124.
Lamb, S. (2006), Shear stresses on megathrusts: Implications for mountain building behind subduction zones, *J. Geophys. Res.*, *111*, B07401, doi:10.1029/2005JB003916.
Mancktelow, N. S. (1995), Nonlithostatic pressure during sediment subduction and the development and exhumation of high-pressure metamorphic rocks, *J. Geophys. Res.*, *100*(B1), 571–583, doi:10.1029/94JB02158.
Mancktelow, N. S. (2008), Tectonic pressure: Theoretical concepts and modelled examples, *Lithos*, *103*(1-2), 149–177.
McIntosh, K. D., E. A. Silver, I. Ahmed, A. Berhorst, C. R. Ranero, R. K. Kelly, and E. R. Flueh (2007), The Nicaragua convergent margin, in *The Seismogenic Zone of Subduction Thrust Faults: Part III*, edited by T. H. Dixon and J. C. Moore, pp. 257–287, Columbia Univ. Press, New York.
Mochizuki, K., T. Yamada, M. Shinohara, Y. Yamanaka, and T. Kanazawa (2008), Weak interplate coupling by seamounts and repeating M similar to 7 earthquakes, *Science*, *321*(5893), 1194–1197.
Moreno, M., C. Haberland, O. Oncken, A. Rietbrock, S. Angiboust, and O. Heidbach (2014), Locking of the Chile subduction zone controlled by fluid pressure before the 2010 earthquake, *Nat. Geosci.*, *7*(4), 292–296.
Nur, A., G. Mavko, J. Dvorkin, and D. Galmudi (1998), Critical porosity: A key relating physical properties to porosity in rocks, *Leading Edge*, *17*, 357–362.
Petrini, K., and Y. Podladchikov (2000), Lithospheric pressure-depth relationship in compressive regions of thickened crust, *J. Metamorph. Geol.*, *18*(1), 67–77.
Ranero, C. R., and R. von Huene (2000), Subduction erosion along the Middle America convergent margin, *Nature*, *404*(6779), 748–752.
Ranero, C. R., I. Grevemeyer, H. Sahling, U. Barckhausen, C. Hensen, K. Wallmann, W. Weinrebe, P. Vannucchi, R. von Huene, and K. McIntosh (2008), Hydrogeological system of erosional convergent margins and its influence on tectonics and interplate seismogenesis, *Geochem. Geophys. Geosyst.*, *9*, Q03S04, doi:10.1029/2007GC001679.
Ruh, J. B. (2016), Submarine landslides caused by seamounts entering accretionary wedge systems, *Terra Nova*, *28*(3), 163–170.
Ruh, J. B., T. Gerya, and J. P. Burg (2013), High-resolution 3D numerical modeling of thrust wedges: Influence of décollement strength on transfer zones, *Geochem. Geophys. Geosyst.*, *14*, 1131–1155, doi:10.1002/ggge.20085.
Ruh, J. B., T. Gerya, and J. P. Burg (2014), 3D effects of strain vs. velocity weakening on deformation patterns in accretionary wedges, *Tectonophysics*, *615*, 122–141.

Sallares, V., and C. R. Ranero (2005), Structure and tectonics of the erosional convergent margin off Antofagasta, north Chile (23°30′S), *J. Geophys. Res.*, *110*, B06101, doi:10.1029/2004JB003418.

Sallares, V., A. Melendez, M. Prada, C. R. Ranero, K. McIntosh, and I. Grevemeyer (2013), Overriding plate structure of the Nicaragua convergent margin: Relationship to the seismogenic zone of the 1992 tsunami earthquake, *Geochem. Geophys. Geosyst.*, *14*, 3436–3461, doi:10.1002/ggge.20214.

Schmeling, H., A. Y. Babeyko, A. Enns, C. Faccenna, F. Funiciello, and T. Gerya (2008), A benchmark comparison of spontaneous subduction models—Towards a free surface, *Phys. Earth Planet. Inter.*, *171*(1-4), 198–223.

Scholz, C. H., and C. Small (1997), The effect of seamount subduction on seismic coupling, *Geology*, *25*(6), 487–490.

Schurr, B., et al. (2014), Gradual unlocking of plate boundary controlled initiation of the 2014 Iquique earthquake, *Nature*, *512*(7514), 299–302.

Singh, S. C., et al. (2011), Aseismic zone and earthquake segmentation associated with a deep subducted seamount in Sumatra, *Nat. Geosci.*, *4*(5), 308–311.

Smith, D. K., and T. H. Jordan (1988), Seamount statistics in the Pacific Ocean, *J. Geophys. Res.*, *93*(B4), 2899–2918, doi:10.1029/JB093iB04p02899.

Spinelli, G. A., and M. B. Underwood (2004), Character of sediments entering the Costa Rica subduction zone: Implications for partitioning of water along the plate interface, *Isl. Arc*, *13*(3), 432–451.

Timm, C., D. Bassett, I. J. Graham, M. I. Leybourne, C. E. J. de Ronde, J. Woodhead, D. Layton-Matthews, and A. B. Watts (2013), Louisville seamount subduction and its implication on mantle flow beneath the central Tonga-Kermadec arc, *Nat. Commun.*, *4*, 1720, doi:10.1038/ncomms2702.

Ueda, H. (2005), Accretion and exhumation structures formed by deeply subducted seamounts in the Kamuikotan high-pressure/temperature zone, Hokkaido, Japan, *Tectonics*, *24*, TC2007, doi:10.1029/2004TC001690.

Vannucchi, P., C. R. Ranero, S. Galeotti, S. M. Straub, D. W. Scholl, and K. McDougall-Ried (2003), Fast rates of subduction erosion along the Costa Rica Pacific margin: Implications for nonsteady rates of crustal recycling at subduction zones, *J. Geophys. Res.*, *108*(B11), 2511, doi:10.1029/2002JB002207.

von Huene, R. (2008), When seamounts subduct, *Science*, *321*(5893), 1165–1166.

von Huene, R., J. Corvalán, E. R. Flueh, K. Hinz, J. Korstgard, C. R. Ranero, and W. Weinrebe (1997), Tectonic control of the subducting Juan Fernandez Ridge on the Andean margin near Valparaiso, Chile, *Tectonics*, *16*(3), 474–488, doi:10.1029/96TC03703.

von Huene, R., C. R. Ranero, W. Weinrebe, and K. Hinz (2000), Quaternary convergent margin tectonics of Costa Rica, segmentation of the Cocos Plate, and Central American volcanism, *Tectonics*, *19*(2), 314–334, doi:10.1029/1999TC001143.

von Huene, R., C. R. Ranero, and P. Vannucchi (2004), Generic model of subduction erosion, *Geology*, *32*(10), 913–916.

Wang, K. L., and S. L. Bilek (2011), Do subducting seamounts generate or stop large earthquakes?, *Geology*, *39*(9), 819–822.

Wang, K. L., and S. L. Bilek (2014), Invited review paper: Fault creep caused by subduction of rough seafloor relief, *Tectonophysics*, *610*, 1–24.

Wang, K. L., and Y. Hu (2006), Accretionary prisms in subduction earthquake cycles: The theory of dynamic Coulomb wedge, *J. Geophys. Res.*, *111*, B06410, doi:10.1029/2005JB004094.

Watts, A. B., A. A. P. Koppers, and D. P. Robinson (2010), Seamount subduction and earthquakes, *Oceanography*, *23*(1), 166–173.

Yang, H. F., Y. J. Liu, and J. Lin (2012), Effects of subducted seamounts on megathrust earthquake nucleation and rupture propagation, *Geophys. Res. Lett.*, *39*, L24302, doi:10.1029/2012GL053892.

Yang, H. F., Y. J. Liu, and J. Lin (2013), Geometrical effects of a subducted seamount on stopping megathrust ruptures, *Geophys. Res. Lett.*, *40*, 2011–2016, doi:10.1002/grl.50509.

Zeumann, S., and A. Hampel (2015), Deformation of erosive and accretive forearcs during subduction of migrating and non-migrating aseismic ridges: Results from 3-D finite element models and application to the Central American, Peruvian, and Ryukyu margins, *Tectonics*, *34*(9), 1769–1791, doi:10.1002/2015TC003867.

Zhan, Z. W., et al. (2012), Anomalously steep dips of earthquakes in the 2011 Tohoku-Oki source region and possible explanations, *Earth Planet. Sci. Lett.*, *353*, 121–133.